IDEA League

Master of Science in Applied Geophysics

Research Thesis

Body-wave seismic interferometry on passive seismic data for imaging CO_2 reinjection at the Hellisheiði geothermal power plant, Iceland

Sverre Henri Willem Hassing

August 5, 2022

Body-wave seismic interferometry on passive seismic data for imaging CO_2 reinjection at the Hellisheiði geothermal power plant, Iceland

Master of Science Thesis

for the degree of Master of Science in Applied Geophysics at
Delft University of Technology
ETH Zürich
RWTH Aachen University
by

Sverre Henri Willem Hassing

August 5, 2022

Department of Geoscience & Engineering · Delft University of Technology
Department of Earth Sciences · ETH Zürich
Faculty of Georesources and Material Engineering · RWTH Aachen University

Delft University of Technology

Copyright © 2022 by IDEA League Joint Master's in Applied Geophysics:

Delft University of Technology

All rights reserved.
No part of the material protected by this copyright notice may be reproduced or utilized in any form or by any means, electronic or mechanical, including photocopying or by any information storage and retrieval system, without permission from this publisher.

Printed in The Netherlands

IDEA LEAGUE
JOINT MASTER'S IN APPLIED GEOPHYSICS

Delft University of Technology, The Netherlands
ETH Zürich, Switzerland
RWTH Aachen, Germany

Dated: *August 5, 2022*

Supervisor(s):

Deyan Draganov

Martijn Janssen

Committee Members:

Deyan Draganov

Auke Barnhoorn

Florian Wellmann

Abstract

CO_2 and H_2S are reinjected at Hellisheiði, Iceland, to reduce the emissions of greenhouse gases. An active-source seismic campaign was done in July, 2021, to image the reinjection reservoir with various seismic methods for consecutive monitoring. At the same time, passive-source seismic data was recorded for imaging.
We process this passive data with seismic interferometry. For this, an illumination analysis is performed to filter noise panels that are dominated by surface-wave noise and to keep panels dominated by body-wave noise. Afterwards, panels with near-vertical events are autocorrelated to retrieve a zero-offset section. The full set of selected panels is crosscorrelated to retrieve virtual shot records. These are processed with a simple reflection seismological processing workflow to obtain a stacked section.
The results show that the autocorrelated zero-offset sections appear more noisy, but are characterised by higher frequencies, while the crosscorrelated stacked sections are characterised by a lower-frequency content and contain more dipping reflectors. The major, horizontal reflectors correspond between the two types of sections.
A rudimentary interpretation of reflectors is done, based on the two types of sections and compared with a local geological model. This shows that the major lithological differences and the base of the Hengill volcano can be distinguished in the interpreted section.

Acknowledgements

Figure 1: View of the Hellisheiði power plant from the main geophone line.

Firstly, I would like to thank my supervisors, Deyan and Martijn, for the help and support during the last five months and for making it possible to join the field work at Hellisheiði, which was a good combination of enjoyable and educational. I would also like to thank Jens and Gijs for making the stay in Iceland more enjoyable.
I would like to thank Fenna for giving me a place to stay and work for a week and some fresh mountain air and Cara, Teus and Kate who gave comments on the thesis.
The second important factor that made the thesis a reality came from the free time to spend on other things. For this I would like to thank the other students of the Applied Geophysics program (and Max, who might as well be one), who convinced me to continue working; Maureen, as my best friend in years; and Daniël, who I still talk to most days, evena after 19 years.
Lastly, I would like to thank my parents, without whom I wouldn't have done anything, and my sister, even though she stole my room.

Delft University of Technology Sverre Henri Willem Hassing

August 5, 2022

Table of Contents

Abstract v

Acknowledgements vii

Acronyms xv

1 Introduction 1
1-1 CO2 reinjection . . . 1
1-2 Reinjection at Hellisheidi . . . 3

2 The Hellisheidi site 5
2-1 Geology . . . 5
2-2 Local seismicity . . . 8
2-3 Local noise . . . 9

3 Seismic interferometry 11

4 Methods 15
4-1 Acquisition information . . . 15
4-2 Raw data . . . 15
4-3 Filtering . . . 17
4-4 Illumination analysis . . . 19
4-5 Autocorrelations . . . 21
4-6 Crosscorrelations . . . 21

5 Results 23
5-1 Illumination analysis . . . 23
5-2 Autocorrelations . . . 25
5-3 A new filter . . . 27
5-4 Crosscorrelations . . . 28

6 Discussion **31**
6-1 Illumination analysis 31
6-2 Zero-offset sections 32

7 Conclusion **35**

Bibliography **37**

A Extra sections **43**
A-1 Cross line sections 43
A-2 Full sections 45

B Slope correction **51**

C Research module **55**

List of Figures

1 View on Hellisheiði vii

2-1 Large-scale geological features of Iceland 5
2-2 Geological sections below survey area 7
2-3 Recorded earthquakes in Iceland 8
2-4 Acquisition geometry of the survey 10

3-1 The basic principle of seismic interferometry 12

4-1 Example of a noise panel 17
4-2 Example of a recorded earthquake with amplitude spectrum 18
4-3 Average amplitude spectrum of 8 hours of noise 18
4-4 Test of the implemented Tau-P transform 20

5-1 Results of illumination analysis with initial filter through time 23
5-2 Histogram with results of illumination analysis with initial filter 24
5-3 Zero-offset section gotten from autocorrelations with initial illumination analysis . . 25
5-4 Zero-offset section gotten from autocorrelations with initial illumination analysis with bandpass filter applied and zero-offset section from second illumination analysis 26
5-5 Results of the illumination analysis with bandpass filter plotted through time 27
5-6 Histogram of results of illumination analysis with bandpass filter 28
5-7 Common-source gather and common-midpoint gather created by crosscorrelating and stacking noise data 29
5-8 Stacked section based on common-midpoint gathers with NMO correction 30

6-1 Interpreted sections on main and cross line 33

A-1 Cross line zero-offset section from autocorrelations based on initial illumination analysis 43

A-2 Cross line zero-offset section from autocorrelations based on initial illumination analysis with bandpass filter applied afterwards 44
A-3 Cross line zero-offset section from autocorrelations based on second illumination analysis with bandpass filter 44
A-4 Cross line stacked section based on common-midpoint gathers after NMO correction 45
A-5 10 s section for main line from autocorrelations 46
A-6 10 s section for cross line from autocorrelations 47
A-7 10 s section for main line from crosscorrelations 48
A-8 10 s section for cross line from crosscorrelations 49

B-1 Elevation of stations with linear fit 51
B-2 Terms defined for slope correction calculations 52
B-3 Results of slope correction 54

List of Tables

2-1 Earthquake events during recording 9

4-1 Acquisition parameters of the survey. 16

5-1 Velocity picks for NMO correction 28

Acronyms

CCS Carbon Capture and Storage

CMP Common MidPoint

DAS Distributed Acoustic Sensing

ECEF Earth Centred, Earth Fixed

EVZ Eastern Volcanic Zone

GHG GreenHouse Gases

HWC Helically Wound Cable

NMO Normal Move-Out

RMS Root Mean Square

RPVZ Reykjanes Peninsula Volcanic Zone

SI Seismic Interferometry

SISZ South Island Seismic Zone

SUCCEED Synergetic Utilisation of CO_2 storage Coupled with geothermal EnErgy Deployment

TRBI Time Reversal Before Integration

TWT Two-Way Traveltime

WVZ Western Volcanic Zone

Chapter 1

Introduction

1-1 CO_2 reinjection

Emission of GreenHouse Gases (GHG), specifically CO_2, is the main driver of anthropogenic climate change (IPCC, 2018, Oelkers and Cole, 2008). Power generation with fossil fuels is the largest contributor to GHG emission, making various alternatives that reduce emissions of interest (IPCC, 2005). One of these is geothermal energy.
This method extracts thermal energy from the subsurface, primarily by drawing liquid from reservoirs and utilising the elevated temperature. Geothermal systems can be divided into two groups. Moderate-temperature geothermal systems characterise reservoirs with temperatures between 70 and 160°C and have enough permeability from porosity or fracturing. High-enthalpy geothermal systems contain high-temperature fluid (typically > 200°C) and are generally contained in the reservoir by a cap rock. Fluid will rise up by itself and produce steam at the surface after depressurising. Most high-enthalphy systems are associated with volcanism. Although geothermal energy generation provides a large reduction in the emission of GHG compared to the usage of fossil fuels, high-enthalpy systems still have some emissions, primarily of CO_2 and H_2S.
An older weighted average, that is still in use (Fridriksson et al., 2017, O'Sullivan et al., 2021), indicates that geothermal energy generation emits 122 g CO_2/kWh, compared to 315 to 915 g/kWh for different fossil fuels (Bertani and Thain, 2002). The CO_2 output is largely determined by the host rock of the geothermal system. For example, igneous rocks release moderate amounts of CO_2, while carbonates release large amounts. With more geothermal fields being developed, locations with high emissions (> 500 g/kWh) are slowly being put in use (Fridriksson et al., 2017).
In high-enthalpy geothermal systems, GHG are also emitted naturally, meaning that a fair comparison needs to subtract the amount emitted if no power plant had been built from the emissions of the power plant itself. This exact amount is unclear, but could be zero (Ármannsson et al., 2005, O'Sullivan et al., 2021). In any case, the GHG emissions are significantly lower than those of fossil-fuel power generation.
With the aim to reduce GHG emissions globally, geothermal power generation can still be

of interest at locations with concentrated, high emissions, located close to natural reservoirs. The former makes it suitable for carbon capture, the latter can be interesting for carbon storage. Carbon Capture and Storage (CCS) means either taking CO_2 that would otherwise be emitted or taking CO_2 directly from the atmosphere and storing it to prevent influence on the global climate.
Geological storage is the most prominent method of storage, due to a large capacity and the possibility of very stable storage (Wu and Li, 2020). The main problem is that CO_2 injected as a gas is lighter than water, so buoyant forces cause it to travel upward. Therefore, there needs to be a mechanism that holds the CO_2 trapped underground. For this, there are four main methods, each requiring specific conditions to be met (IPCC, 2005, Benson and Cole, 2008):

- Structural trapping
  After pure CO_2 is injected, an impermeable layer above the injected plume prevents it from travelling back up to the surface. This can also effectively happen in natural formations where CO_2 migration is slow. The amount of time it would take to travel out of the formation is so long, that other trapping mechanisms can occur.

- Capillary trapping
  When water imbibes in a plume of pure CO_2, small amounts of CO_2 remain trapped in the pores, while the rest migrates away.

- Solubility trapping
  Injected gases slowly start to dissolve in pore water. If the pore water does not travel to the surface, this means that the CO_2 remains underground. The rate of dissolution depends on the pressure, temperature, salinity and contact area of the two phases.

- Mineral trapping
  Dissolved CO_2 can react with minerals present, either in the pore water or the surrounding matrix. This method presents the most long-term, stable storage mechanism, but can take a long time to establish.

After injection of pure CO_2, it can take a long time (possibly >1000 years) for a stable storage mechanism to take effect, while the integrity of the cap must remain (IPCC, 2005).
The CarbFix project was set up in 2006 as a cooperation between Reykjavik Energy, the University of Iceland, Columbia University in New York and the Centre National de la Reserche Scientifique in Toulouse (Matter et al., 2011, Carbfix, n.d.). The aims were to both reduce the amount of time required for stable storage of CO_2 and to reduce the cost of the injection process. The project also injected H_2S at the same time for geological storage (Aradóttir et al., 2015).
The project improved traditional injection methods on two fronts. The first was by dissolving the injected CO_2 in the injected fluid before it entered the formation. This was done by releasing it as small gas bubbles in the injection well, where the CO_2 was mixed with, and dissolved in, the injected water (Aradóttir et al., 2015, Sigfússon et al., 2015). It effectively skips the structural and capillary trapping, as solubility trapping is the starting position. There is less of a risk of escape to the surface and reactions with minerals can start earlier.
The second focus of the CarbFix project was injection in young basalt formations. The reactions where CO_2 is made stable mostly require divalent cations. These are made available

in basaltic and ultramafic rocks as they dissolve readily (Aradóttir et al., 2015). Younger basalts, for example, formed in active rift zones, are more fit for storage because they have a higher porosity and contain more faults (Snæbjörnsdóttir et al., 2014). The original pore space is slowly filled with secondary minerals.
For this reason, the CarbFix project ran its trial in Iceland, where abundant young basalt is formed as part of the Atlantic mid-oceanic rift (Snæbjörnsdóttir et al., 2014). To be close to a source of CO_2, the injection happened near the Hellisheiði geothermal power plant. After the trial run, it was found that more than 95 percent of CO_2 was converted to minerals after only two years (Matter et al., 2016).

1-2 Reinjection at Hellisheiði

The Hellisheiði geothermal power plant was built after an extensive exploration of the area and started production, operated by Reykjavik Energy, in 2006 (Durucan et al., 2021). It supplies both heating (200 MW thermal energy) and electricity (303 MW) to the city of Reykjavik (ON Power, n.d.).
For the CarbFix project, the CO_2 produced from the power plant was injected with water at an injection well. The well is 2000-m-deep and located about 3 km to the south of the power plant (Gislason et al., 2010). The target formation is located in the range of 400 m to 800 m under the surface (Sigfússon et al., 2015).
After successful operation, the project was expanded in 2014 and injection rates were increased in the CarbFix2 project (Sigfússon et al., 2018). The new injection site is located 1.5 km north of the power plant at Húsmúli and has overtaken the first one in reinjection rate. Multiple injection wells are currently in use at the new injection site (Ratouis et al., 2022). The main well, HN16, has been drilled to a true vertical depth of 1902 m (Snæbjörnsdóttir et al., 2018). The injected fluid was observed with three monitoring wells between 984 m and 1482 m deep at the depth of the main aquifers (Gunnarsson et al., 2018).
The newest project concerned with monitoring the injection at Hellisheiði is the Synergetic Utilisation of CO_2 storage Coupled with geothermal EnErgy Deployment (SUCCEED) project. The aim is to show that reinjection increases geothermal performance and to use new seismic methods for monitoring injected CO_2 (Durucan et al., 2021).
During July 2021, a seismic survey was conducted at the Húsmúli site for the SUCCEED project. The survey included data from 148 three-component SmartSOLO stations, 48 two-component geophones and a Helically Wound Cable (HWC) Distributed Acoustic Sensing (DAS) line. The SmartSOLO stations were placed along a main and cross line, while the other two were placed along the same main line.
An active-source campaign was executed for the survey with a seismic vibrator source, where 59 vibrator points were shot along the main line. During the same week, the SmartSOLO stations and the DAS cable recorded ambient noise. During June 2022, the same active-source survey was repeated, except only the DAS cable recording was performed. As such, the passive survey can only be used for imaging and contribute to the interpretation of the active-source data, but cannot be used for monitoring the reservoir.
This thesis will focus on processing the passive data, recorded on the SmartSOLO geophones, using seismic interferometry to obtain an image of the reservoir where reinjection happens in the CarbFix2 project. As only the passive data from the SmartSOLO geophones is used in this thesis, we will refer to the SmartSOLO geophones stations as

simply stations. The main line is the geophone line that lies parallel to the DAS cable, while the cross line is the geophone line perpendicular to the cable. The exact position is discussed below and shown in figure 2-4.
This thesis will continue by providing more context on the local geology and site characteristics of Hellisheiði. Then, the theoretical background of seismic interferometry is shortly discussed. After this, first we discuss the methods used to process the data, then we present the results of the processing, we describe these results in the discussion and finally draw conclusions.

Chapter 2

The Hellisheiði site

2-1 Geology

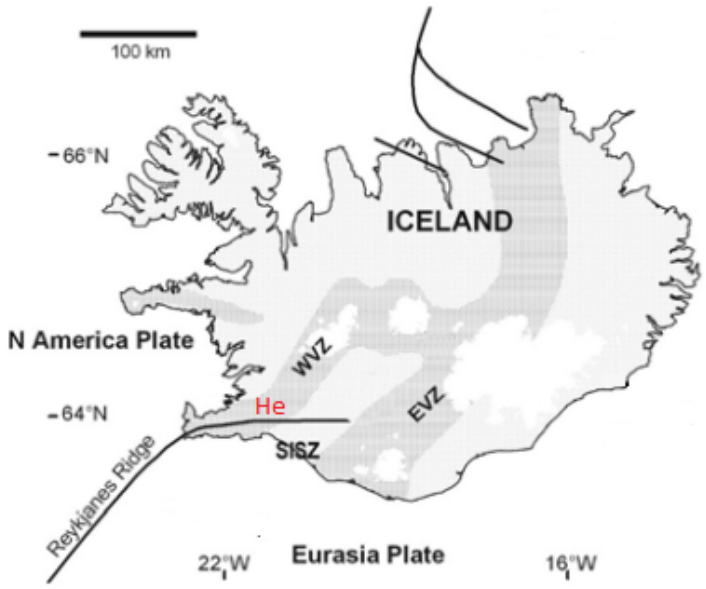

Figure 2-1: Important seismic features of Iceland. The plate boundary between the North American and Eurasian plates is indicated in black bold lines and as the dark, shaded zone. The Hengill volcanic system is indicated in red. Nearby features are: EVZ *Eastern Volcanic Zone*, He *Hengill volcanic system*, WVZ *Western Volcanic Zone*, SISZ *South Island Seismic Zone*.
Image adapted from Einarsson (2008).

Iceland is located at a geologically special position, lying on top of the Atlantic rift and the Icelandic hotspot. The divergence zone of the rift becomes broader underneath Iceland and

contains various different volcanic systems. The plate boundary reaches land at the Reykjanes peninsula and extends along it (see fig. 2-1).
From there, plate movement is accommodated by two parallel rift zones, the Western Volcanic Zone (WVZ) and Eastern Volcanic Zone (EVZ). Between these rift zones lies the transform South Island Seismic Zone (SISZ) (Einarsson, 2008).
At the triple junction formed by the WVZ, the SISZ and the Reykjanes Peninsula Volcanic Zone (RPVZ), lies the Hengill volcanic system. This is a larger system that contains fissure vents, a series of smaller volcanoes, craters and a large, central volcano, also called the Hengill volcano. The Hellisheiði site lies on the southern flank of this volcano.
The base of the volcano is found around 1200-1500 m depth. This is a lava succession that is highly altered and cut through by intrusions and originates from a nearby, extinct volcano (Snæbjörnsdóttir et al., 2018). This base has been dated to about 0.4 Ma, giving a maximum age to the volcano (Franzson et al., 2010).
The Hengill volcano itself consists primarily of two different lithologies: hyaloclastic and lava. Hyaloclastic (glassy) formations form when lava erupts beneath ice during glacial periods. Lava sequences form during interglacial periods, when the lava can flow over the surface. These flows mostly end up in local depressions (Gebrehiwot et al., 2010).
Consequently, the topographically higher volcano consists of hyaloclastic formations, while the low areas, such as the Hellisheiði area, were filled up with successions of hyaloclastic formations and lava sequences. Intrusions can be found from 500 m below the surface, while becoming more common around 1500 m below the surface. These intrusions create significant permeability when formed (Snæbjörnsdóttir et al., 2018).
The centre of the volcano is dominated by a large fissure swarm, associated with the rifting zones, that forms a graben structure. Two recent eruptions (5 and 2 ka) have created important sets of fissures, trending NNE-SSW. Oriented along these features are large, subvertical faults that could represent the western edge of the fissure zone (Hardarson et al., 2010). These together account for a total throw of 300 m (Franzson et al., 2010). The second major set of fissures trends roughly NE-SW and is associated with the transform SISZ (Franzson et al., 2010).
The combination of volcanic activity and the permeability created by these structures results in several naturally occuring geothermal reservoirs in the area (Helgadóttir et al., 2010). Tracer tests have shown that the NNE-SSW features are the major facilitators for flow of subsurface liquids. The NE-SW fissures lie perpendicular to the flow direction and form barriers to flow (Ratouis et al., 2019).
The presence of water and heat also results in hydrothermal alteration of minerals. Thermal alteration zones present a proxy for the local geothermal gradient. This varies between 80 and 250 °C/km in the Hengill field (Franzson et al., 2005, Alfredsson et al., 2013).
A schematic geological model of the area can be found in figure 2-2 (Janssen, pers. comm. June, 2022). The models show the main lithologies, geological features and locations of injection wells. The main features are two prominent lava sequences around sea level and at 400 m below sea level. Around these lava sequences, hyaloclastites can be found. Around 1600 m below sea level, the hyaloclastites disappear and the lava sequences become the main lithology. This deeper part is also cut through by several intrusions, which are oriented subvertically. The boundary between the hyaloclastites and lava sequences around 1600 m depth likely indicates the base of the Hengill volcano.
Two injection wells are projected onto the geological sections. This shows that the deepest injection occurs around the base of the volcano, around 1900 m below the surface.

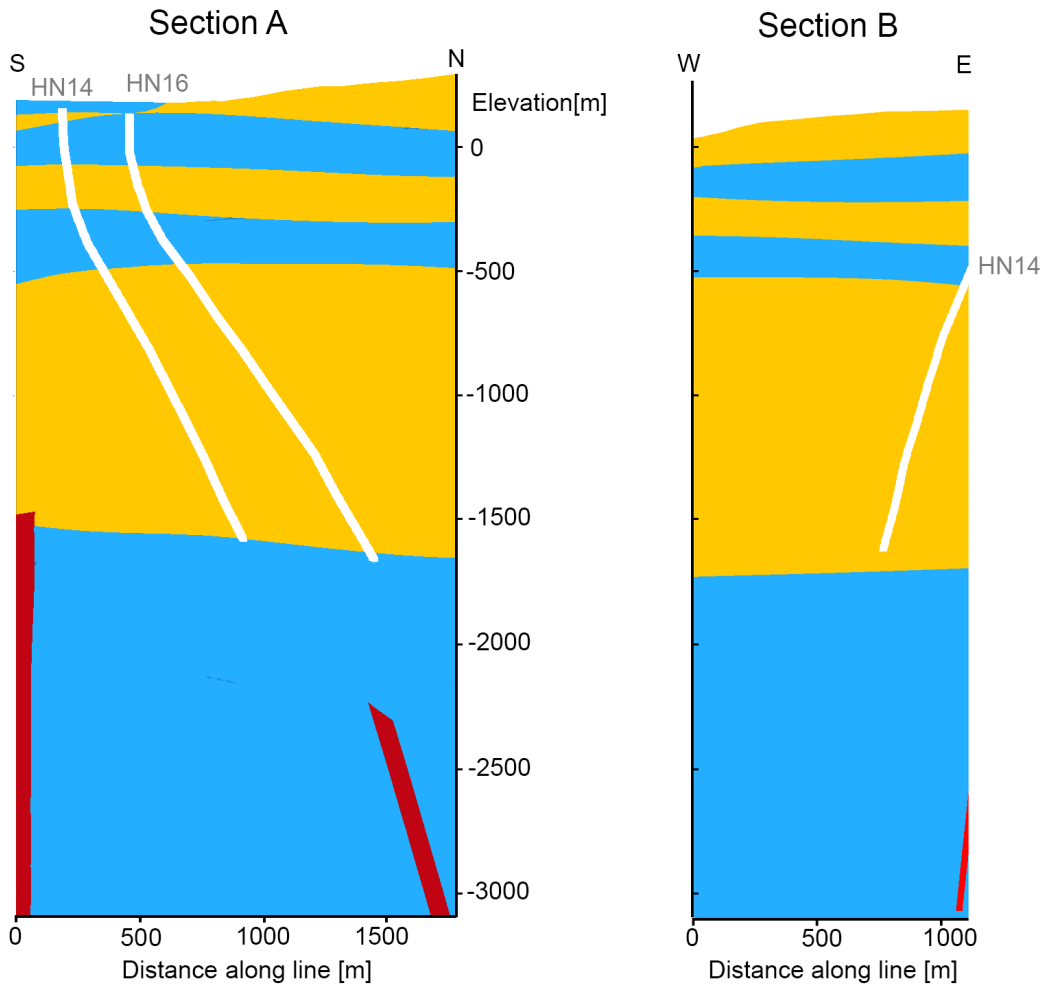

Figure 2-2: Schematic geological profiles underneath the survey area. Section A aims to follow the main geophone line, while section B is oriented along the cross line. Exact locations of the profiles are indicated in figure 2-4. Yellow indicates hyaloclastites, blue indicates lava sequences and red indicates intrusions. Two of the injection wells close to the profiles (HN14 and HN16) are projected onto the profile as white lines.

2-2 Local seismicity

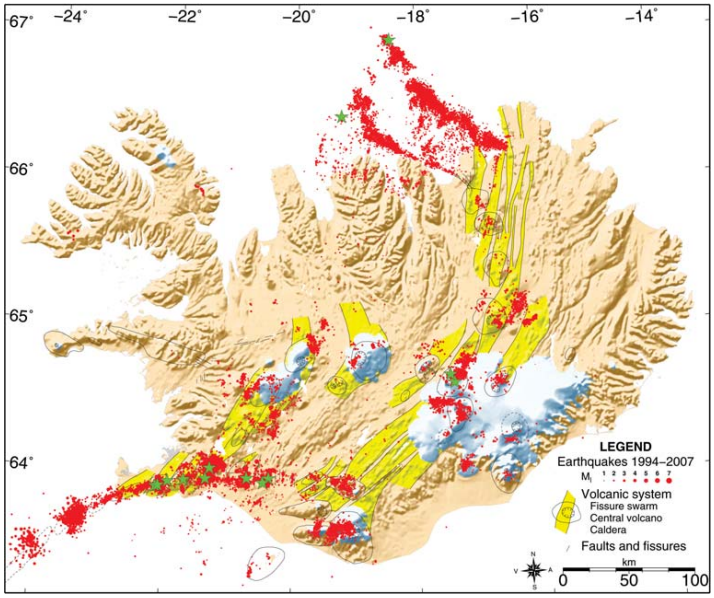

Figure 2-3: Map of local seismic events. Red dots are earthquakes with local moment magnitude $M_l > 1$ recorded between 1994 and 2007 by the South Island Lowland seismic acquisition system. Green stars indicate earthquakes with a magnitude $M_l > 5$. Map taken from Jakobsdóttir (2008).

The Hengill volcanic system and the structures that form the triple junction are one of the main contributors to seismic activity in Iceland (Jakobsdóttir, 2008). Figure 2-3 displays a map showing the distribution of seismic activity in Iceland between 1994 and 2007. During this period, 40% of the recorded earthquakes in Iceland were located within the Hengill area (Jakobsdóttir, 2008). Different earthquake swarms and sequences have also occurred in the area, accompanied by strong ($M_l \geq 5$) earthquakes. Most of the activity during this time was caused by rifting and volcanic activity.

The seismicity in the Hengill area changed after the geothermal power plant began operations. Both injection and production wells are associated with clusters of seismicity. Duran Neme (2021) found that the cluster under the CarbFix2 injection site at Húsmúli was the most active, with 27% of the recorded events being linked to this site. The earthquakes are clustered around two depths - 2 and 5 km. The shallower depth is likely associated with reinjection, while the deeper one is linked to natural seismicity.

During the week that the passive survey was executed, there were 40 recorded earthquakes with a magnitude above 2.0 (VolcanoDiscovery, n.d.). There was also a very strong earthquake of magnitude 8.2 in Alaska, more than 6000 km from Hellisheiði (USGS, n.d.).

Time (UTC)	Magnitude	Latitude	Longitude	Nearby location
2021-07-23 09:58	2.5	64.133N	21.368W	Hellisheiði, Iceland
2021-07-26 18:55	2.2	64.102N	21.332W	Hellisheiði, Iceland
2021-07-27 19:02	4.0	64.620N	17.450W	Bárðarbunga, Iceland
2021-07-27 22:12	4.5	64.621N	17.358W	Bárðarbunga, Iceland
2021-07-28 23:40	2.1	63.962N	21.797W	Hafnarfjörður, Iceland
2021-07-29 06:15	8.2	55.364N	157.888W	Chignik, Alaska
2021-07-29 06:25	5.0	66.320N	17.340W	Húsavík, Iceland

Table 2-1: A selection of earthquakes that happened during the recording of the passive survey that have a high-enough magnitude or have their epicentre close enough to the recording site to be recognisable in the data. Via VolcanoDiscovery (n.d.) and USGS (n.d.).

2-3 Local noise

To look at the possible sources of noise during the recording of the data, we will zoom in even further to the Hellisheiði power plant itself and the nearby injection field for CarbFix2. These are shown on figure 2-4. The injection wells and geophone lines are located above the target reservoir. The power plant itself is depicted as the group of buildings around the red pin.
Below, a list is presented of possible noise sources in the environment around the geophone lines:

- The geophones are located on a larger hill with little vegetation (only grass and moss). This gives little protection against the wind.
- During the first two days of recording (24 and 25th of July, 2021) a large storm passed over the field location, possibly producing more noise.
- The field location is near the coast, meaning that microseism noise (generated by waves) is highly likely to be present (Aster et al., 2010). This microseism energy is recorded at frequencies of < 0.25 Hz with peaks at 0.14 Hz and 0.071 Hz (Gualtieri et al., 2013).
- The power plant itself also emits significant amounts of acoustic noise depending on its operation. When steam is vented to the air, this creates a loud, rumbling sound that can be heard clearly through the entire field.
- The purple pin on the image indicates the location of a CO_2 air capture plant that was being expanded at the time of recording. The construction work can induce both acoustic and surface-wave noise.
- The Iceland national road 1 (Þjóðvegur 1) runs 1.75 km south of the main line. The road itself is not busy at this location and mostly used by smaller vehicles. This means that the road is unlikely to be a large source of noise.
- The grounds of the power plant itself, however, contain roads that come closer to the geophone lines and are used by the larger construction traffic. This can be a source of surface-wave noise.

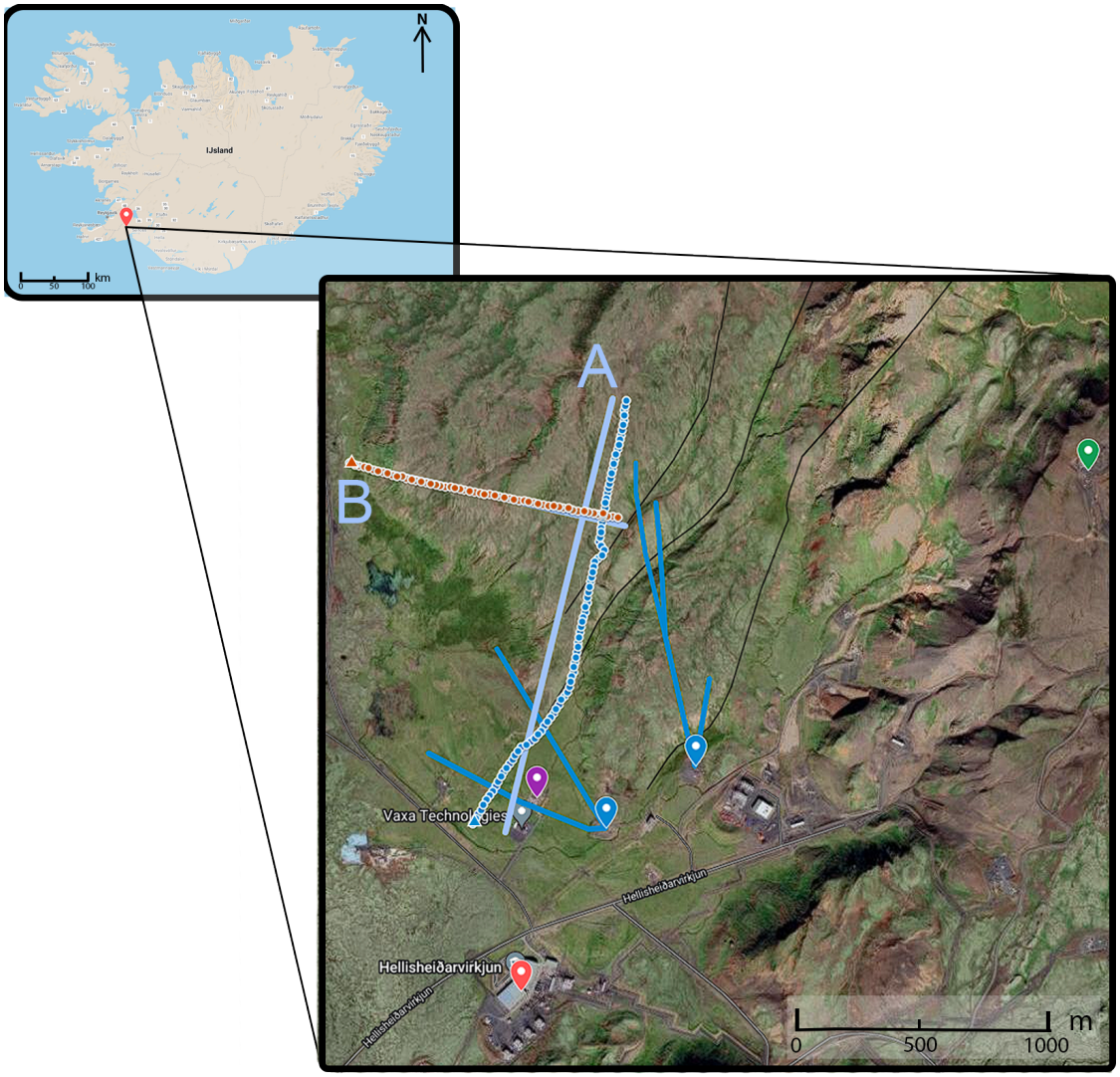

Figure 2-4: Location of the survey in Iceland at the Hellisheiði powerplant and acquisition geometry. Every circle indicates a SmartSOLO station. The blue circles belong to the main line (line 0), while the red circles belong to the cross line (line 1). The triangles indicate the base of each line. The light blue lines indicate the geological sections in figure 2-2. The red pin indicates the power plant, the dark blue lines - the injection well traces, the green pin - the monitoring wells, the purple pin - the CO_2 air capture plant and the black lines - fault traces. Well traces and faults are based on Ratouis et al. (2022).
Source: Google, ©2022, CNES / Airbus, Maxar Technologies

Chapter 3

Seismic interferometry

We also discussed Seismic Interferometry (SI) and the applicability of different sources for the present work in Hassing (2022), included as appendix C. There, it was concluded that SI with local microseismicity is the best technique to use for the survey. Hence, the other SI techniques will not be discussed. The basics of SI will be discussed in more detail, so that this work may stand on its own.

SI is a method that retrieves the seismic response from a virtual source at one receiver position by crosscorrelating the recording at that receiver position with the records from other receivers. Considering an event that first hits one receiver, propagates further and hits another receiver, the crosscorrelation effectively eliminates the shared path.
This means that the result shows the signal as if the source were at the first receiver location and propagated to the second receiver location. Because there is no actual source at the first receiver, it is called a virtual-source location.

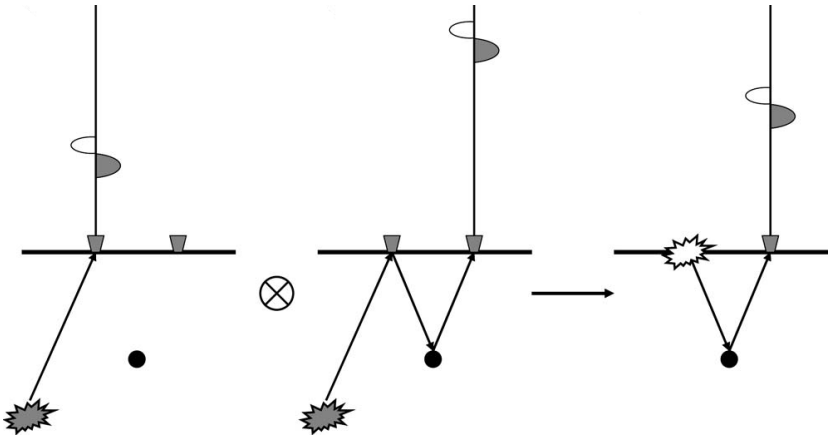

Figure 3-1: Image showcasing the basic principle behind seismic interferometry (SI) with body waves. The triangles are receivers. The recorded traces are shown above each receiver. Crosscorrelation is indicated with $\otimes$. The effect is that the shared path is eliminated and a reflection recording is retrieved.
Image taken from Wapenaar et al. (2010).

It can be implemented in different ways for different types of waves and receiver configurations. A separation can be made between surface-wave and body-wave methods. For imaging of a deeper reservoir, body-wave imaging is the obvious, preferred choice.
To visualise this concept (see also fig. 3-1), imagine a source somewhere at an arbitrary depth. The wave generated by the source propagates along a ray path upwards and reflects off the surface at the first receiver location. The wave propagates through the subsurface and reflects off some reflector within the reservoir. Finally, the wave reaches the second receiver.
SI removes the shared path, i.e. from the original source position to the surface at the first receiver location. What remains is a trace used for reflection seismology. Waves from a (virtual) source at the surface propagate into the subsurface and are reflected. The reflected waves are recorded at a receiver location.
For the full derivation of the Green's function representation with noise sources, see Wapenaar and Fokkema (2006), specifically their equation 87. Several assumptions are made during the process, which is important to take note of:

- The medium is lossless;
- The part of the medium containing the receivers is surrounded by a boundary with sources on them;
- The medium outside of this boundary is isotropic with a certain density ρ and seismic velocity c_p, where the p can indicate P- or S-wave velocity;
- The present noise sources are uncorrelated for different components and different locations;
- The power spectrum of all sources is the same, except for a normalisation factor.

In reality, there will not be fully enclosing sources. If one takes the ray path that ends up reaching both receivers, the stationary-phase zone around the ray only contributes to the Green's function (Snieder, 2004). This means that more realistic scenarios should also work.

From here, we take equation 87 from Wapenaar and Fokkema (2006)

$$\left\{G^{v,f}_{p,q}\left(\mathbf{x}_A,\mathbf{x}_B,t\right)+G^{v,f}_{p,q}\left(\mathbf{x}_A,\mathbf{x}_B,-t\right)\right\}*S(t)\approx\frac{2}{\rho c_P}\left\langle v^{obs}_p(\mathbf{x}_A,t)*v^{obs}_q(\mathbf{x}_B,-t)\right\rangle, \tag{3-1}$$

and explain the different elements of the equation one by one:

- $\boldsymbol{x}_A, \boldsymbol{x}_B$ — Location vectors for receivers A and B.
- $G(\boldsymbol{x}_1, \boldsymbol{x}_2, t)$ — The Green's function as the impulse response of the medium recorded at location 1, caused by a source at location 2, varying through time.
- v, f — Indicate the observed (v) and source (f) quantities. The observed quantity is a particle velocity and the source quantity is a force.
- p, q — The direction of the observed and source quantities, where p gives the direction of the measured quantity and q the direction of the source quantity.
- $f(t) * g(-t)$ — The $*$ indicates a convolution of the two time series, the reversed time in the second series converts it to a correlation.
- $S(t)$ — The autocorrelation of the noise source wavelet.
- $\frac{2}{\rho c_p}$ — This term contains the density and seismic velocity along the enclosing surface. It serves as a power normalisation. In a practical case, these are not known, so they will be ignored.
- $\langle \cdots \rangle$ — The brackets indicate ensemble averaging. Similar to Draganov and Ruigrok (2014), in a practical case, this can be exchanged by a summation over recorded noise panels.
- $v^{obs}(\boldsymbol{x}_1, t)$ — Is the recorded noise at location 1, separated into noise panels. Each panel is a short section of the recorded noise.

With the small adjustments from the ensemble averaging we obtain

$$\left\{G^{v,f}_{p,q}\left(\mathbf{x}_A,\mathbf{x}_B,t\right)+G^{v,f}_{p,q}\left(\mathbf{x}_A,\mathbf{x}_B,-t\right)\right\}*S(t)\approx\sum_{i=1}^{N}v^{obs}_p(\mathbf{x}_A,t)*v^{obs}_q(\mathbf{x}_B,-t). \tag{3-2}$$

To put this into words, this equation dictates that the observed response at receiver A correlated with the response at receiver B, for multiple panels added together, approximates the Green's function with a virtual source at receiver B, recorded at receiver A, with a causal and an acausal version, convolved with a source signature.
This source signature is the autocorrelated source wavelet. To obtain the Green's function,

the source signature should be removed from the record.
The final step is to combine the causal part and acausal part into a final Green's function, in which both parts contribute. The simplest method is to add a time-reversed version of the acausal part to the causal part. It is, however, better to look at the direction the energy is arriving from and make a decision based on this information (Ruigrok et al., 2010).
At receiver positions that are located in the direction of arriving energy from the virtual-source position, the arrival is recorded in the causal Green's function. At receiver positions located on the other side of the virtual-shot location, the arrival is recorded in the acausal Green's function with an opposite dip. Switching the causal and acausal versions at the virtual-source location effectively balances the illumination.
As mentioned above, body-wave SI is used to image deeper structures. In practice, surface-wave energy dominates most of the panels during noise recordings. Ideally, the surface-wave energy would be filtered out to obtain data with only body-wave arrivals. Practically, it is a lot easier to select panels from the noise data where body-wave energy dominates.
One method of selecting panels is by performing an illumination analysis on each panel (Almagro Vidal et al., 2014). This results in the ray parameter of the dominant event in the panel. The ray parameter indicates from which direction the event arrived at the measuring location. The ray parameter can also be interpreted as the slowness of the event, the inverse of the apparent velocity.
Surface waves have a relatively low apparent velocity, equivalent to a high slowness. Body-wave events, arriving from below, have a relatively high apparent velocity, so a low slowness. This means that slowness can be used to distinguish between the two types of waves.
Crosscorrelating all of the traces in the panel with a single master trace results in a virtual common-shot gather. This can be repeated for every receiver location to obtain a full data set with virtual shots at every receiver location. With a reflection seismology processing workflow, the data set is converted into an approximated zero-offset section.
The second advantage of selecting panels after an illumination analysis is that it can be used to only select events that arrived (approximately) vertically (Oren and Nowack, 2016, Polychronopoulou et al., 2020). In a horizontally-layered subsurface, the recordings that result from vertically propagating waves are zero-offset traces. Because of the reliance on vertically propagating waves, this method does have problems imaging dipping reflectors.
Because the vertically propagating events will reach the other stations at nearly the same time, no crosscorrelations have to be performed. This means that the autocorrelation of each trace is enough information. It is still necessary to stack over multiple noise panels, to ensure a better signal-to-noise ratio.

Chapter 4

Methods

The data processing is carried out using Python 3.9.7. The basic importing and plotting of data is done with Obspy 1.3.0 (Beyreuther et al., 2010, Krischer et al., 2015). This package focuses on applications for global seismology, so, for the purpose of this thesis new functions have been written. These can be accessed at Github. The scripts used to process the data and to generate the figures in this thesis are also provided. The raw noise data is not provided, as the data set is too large to include.

4-1 Acquisition information

The data were collected at the Húsmúli field near the Hellisheiði geothermal plant in Iceland. For the exact position and acquisition geometry, see figure 2-4. The data was collected using three-component seismometers with 148 station locations. The three components are oriented towards the north (N), towards the east (E) and vertically (Z). The seismometers are spread over two lines: the main line (also line 0), roughly oriented N-S, and the cross line (line 1), roughly oriented E-W. The spacing between stations was roughly 20 m. For more specific acquisition parameters, see table 4-1.
The data were collected between the 23rd and 31st of July 2021. Not all of the stations started recording at the same time. The time when all of the stations were active lasted from 11:54 on the 24th to 9:00 on the 30th of July. Only this time frame will be used for the processing. There are some time instances during which the recording of some of the stations malfunctioned. This adds up to about 50 minutes. These parts of the data are therefore left out of the processing. This means that a total of 5 days, 20 hours, 17 minutes and 40 seconds of data is available to process.

4-2 Raw data

The data from the survey is delivered as separate .miniseed files for each station, component and day. Opening an hour of data for all stations, requires opening each 24-hour segment

Model seismometer	SmartSolo IGU-16HR 3C 5Hz	
Firmware version	V1.0.5.6kp	
Components	N, Z, E	
Sampling rate	1000 Hz	
	Line 0	Line 1
Amount of stations	92	56
Orientation	NNE-SSW	WNW-ESE
Length	1.84 km	1.09 km
	First station	Last station
Starting time	2021-07-23 00:01:15	2021-07-24 11:54:21
End time	2021-07-30 08:59:55	2021-07-31 00:00:00
Active time	5 days, 21 hours, 6 min., 20s	
Eff. active time	5 days, 20 hours, 17 min. and 40 s	

Table 4-1: Acquisition parameters of the survey.

for 148 stations and then cutting down to the required time. This was double if the selected hour crosses midnight. To make the data more manageable to work with, especially for later processing, the files were combined for every station and cut up for each half hour.
Together with the seismic data, the geographical positions of the stations were provided as WGS84 coordinates. To determine the distances between the stations, the coordinates are transformed to an Earth Centred, Earth Fixed (ECEF) Cartesian system. This means that these distances ignore the curvature of Earth, but with a maximum distance of 1.84 km, this will not give significant errors.
With the seismic data and the geographical positions, the noise panels can be analysed. An example of a panel is shown in figure 4-1. In this panel, there are several clearly visible events - where some arrive with a hyperbolic move-out, while others arrive as horizontal lines in the records.

An important consideration for the processing is how long to make the noise panels that will be used for the correlations. The panel length is the same as the final shot record length. It should at least include the Two-Way Traveltime (TWT) to the deepest reflector desired. A longer recording of the same noise source increases the signal-to-noise ratio. On the other hand, a longer recording has a higher chance of including noise from a different noise source, thus losing signal.
This means that the panel window length should have a balanced length. The target reservoir for injection lies at 2 km depth. To be safe, a low seismic velocity is assumed. Based on lab experiments with samples collected at the time of recording, a lower seismic velocity for P-waves of 1800 m/s is deemed to be reasonable (Janssen et al., 2022). This gives a minimum panel length of 2.2 s.
To ensure that the full reservoir is imaged, this length is slightly extended to 3.0 s. To also include two extra multiples of layers in the reservoir, the length is multiplied by three. Finally, this length is rounded up to 10 s to make the computations easier.
This length is not unreasonable, considering the amount of data available and the application it is used for. Other, similar cases use comparable window lengths (Almagro Vidal et al., 2014, Boullenger et al., 2015, Panea et al., 2014); however an overlap in panels is often used. This provides more granularity, so it should provide more body-wave-dominated panels. Using no

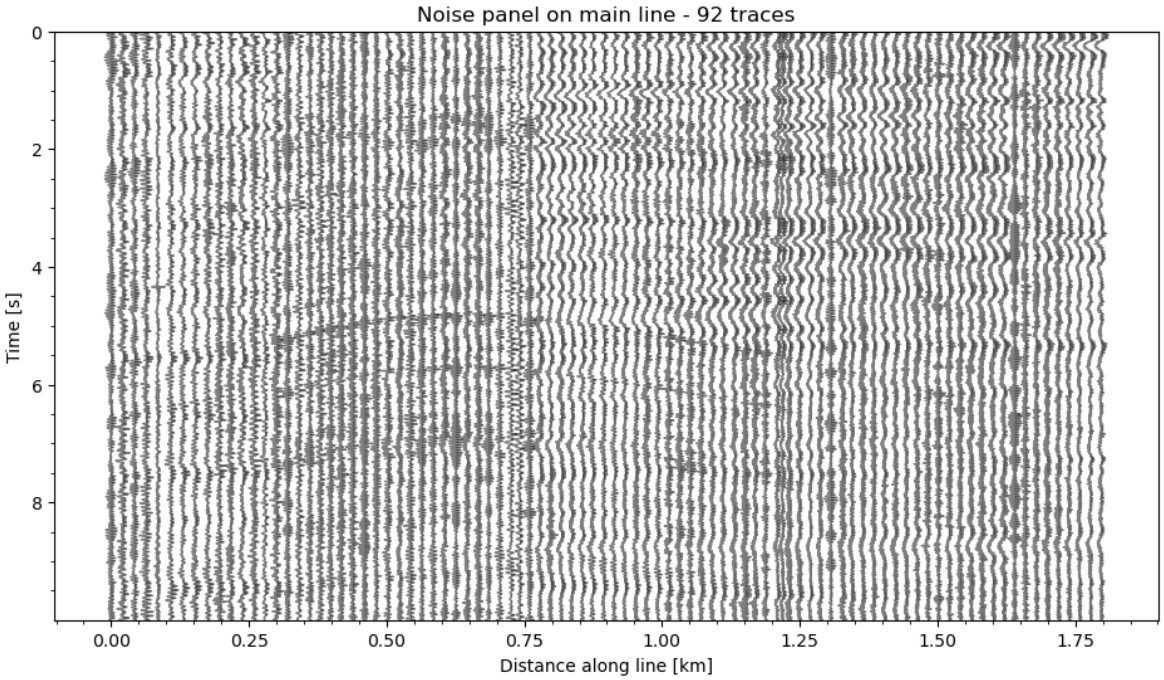

Figure 4-1: Noise panel showing the recorded Z-component along the main line starting at 22:12:50 on 2021-07-27 and lasting 10 s. Different events are clearly visible in the panel. There are some that arrive as horizontal lines, while others show hyperbolic moveout.

overlap gives exactly 50506 panels, representing 5 days, 20 hours, 17 minutes and 40 seconds of data.
An overlap would increase the number of panels too much to be feasible for this work. However, the large amount of time available still means that enough panels can be selected without an overlap.

4-3 Filtering

Some frequency bands are dominated more by noise than by the wanted signal. By filtering these out the overall image quality can be improved. As the target event to locate later on is local seismicity, we will start by looking at known earthquake arrivals. A small list of those can be found in table 2-1. The magnitude M_W 2.2 earthquake near Hellisheiði recorded on the Z-component is shown in figure 4-2.

The amplitude spectrum shows a band of noise that is continuously recorded around 21 Hz. Upon further inspection, a similar line can be seen around 40 Hz, but this is overshadowed by the earthquake in the averaged spectrum. These frequency spikes can be observed in more of the noise panels, with sometimes a clear second overtone at 63 Hz. It is possible that these are related to noise from the wind at 21 Hz with overtones at 42 and 63 Hz.
The earthquake itself shows up as a clear, brighter spot between 30 and 40 s. It is mostly recorded in a band between 3 and 42 Hz. The analysis of the noise continues by looking at the average amplitude spectrum over a larger amount of time. This can be found in figure 4-3.

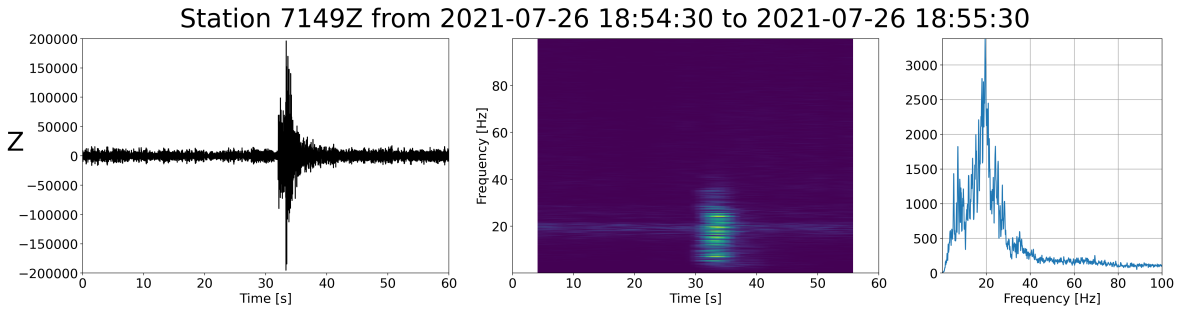

Figure 4-2: The earthquake of 2021-07-26 18:55 as recorded by the station at the crossing of the two lines for the Z-component. The middle panel shows the amplitude spectrum based on a moving window. The right panel shows the average amplitude spectrum over the full minute shown.

The general trend is a large peak around 20 Hz that slowly tapers off towards higher frequencies. Various narrow-frequency peaks are additionally observed. While the peaks at 21 Hz and 42 Hz are clear, the presumed peak at 63 Hz is not visible. The peak at 21 Hz is also part of the larger trend. The peak at 50 Hz is likely related to the frequency of the electrical network.
Some panels are dominated by noise with frequencies below 1 Hz. This does not clearly show up in the averaged spectrum, where there is only a small bump below 1 Hz.
A possible explanation for the low-frequency noise is microseism noise, commonly found in this frequency range. As there is not much other signal found in this range, it can safely be cut out.

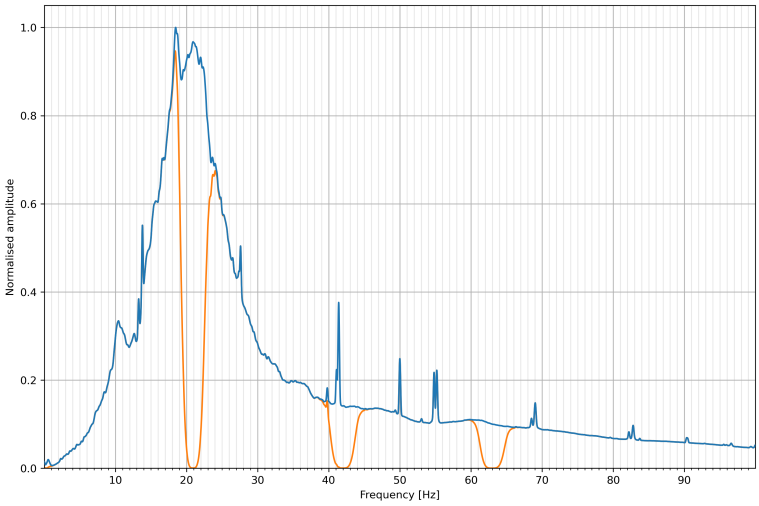

Figure 4-3: Averaged amplitude spectrum of 8 hours of noise. The blue line indicates the average amplitude spectrum of the original noise panels. The orange line indicates the average amplitude spectrum of the same noise with the initial filter applied. This consists of a low-cut filter below 1 Hz and three notch filters around 21, 42 and 63 Hz.

To not remove too much signal at first, the initial filtering of the data will be very modest. The peaks at 21, 42 and 63 Hz are filtered out with notch filters, while a low-cut filter will remove everything below 1 Hz.
The notch filters will be implemented as Butterworth filters of order 4 with edge frequencies 2 Hz away from the central frequency. This means that for the 21 Hz peak, the edge frequencies are 19 and 23 Hz. The resulting average spectrum can also be found in image 4-3.
The filter will be reevaluated after the first autocorrelated data is available, after which the

process can repeat with the new filter.

4-4 Illumination analysis

As mentioned, for body-wave SI, the data needs to be filtered from panels that are dominated with surface-wave energy by means of evaluating the direction of the arriving events for each panel. This is done similarly to Panea et al. (2014), by performing illumination analysis on the crosscorrelated panels.
The events that pass through the virtual-source position at time zero in the crosscorrelated panel give the dominant events. Additionally, the slownesses of these events indicate what type of event they could be, and can additionally be used as a measure for the angle of incidence of the event, depending on the medium velocity.
The illumination analysis is done with a simple Tau-P transform. This method, also called a linear Radon or slant-stack transform, computes a simple plane wave decomposition for a horizontally layered medium.
This is carried out by summing the recorded amplitudes along a line in the seismic record, starting from some intercept time (τ). The slope of this line is determined by the slowness (p). The result of the transform gives the summed values for each intercept time and slowness. Or in mathematical terms (Kappus et al., 1990):

$$R\{u(x,t)\} = s(p,\tau) = \int_{-\infty}^{\infty} u(x, \tau + px)dx, \tag{4-1}$$

where $u(x,\tau)$ is the recorded seismic data at a certain location x and time τ, p is the slowness and both $R\{\}$ and $s(p,\tau)$ indicate the Tau-P transform.
The highest value resulting from the transform shows the dominant slowness of the panel. The slowness can also be interpreted as a ray parameter, indicating from which direction the event arrives. Because the dominant event should go through time zero, the only intercept time evaluated is $\tau = 0$.
A low slowness indicates that the angle of incidence is high. If we consider a single line of geophones on a horizontal surface, an event arriving with normal incidence would hit all locations at the same time. This would suggest an infinite apparent velocity (or a slowness of zero).
However, there is still some ambiguity because a surface-wave event with a propagation direction perpendicular to the line would give the same result. For this reason, the Tau-P transform is applied to both lines separately. Only when the slowness indicates a body-wave event on both lines, can the panel be accepted.
A second complication arises from the slight elevation differences in the terrain. Imagine geophones situated on a line with a slight slope; an event propagating vertically would register as being slightly off vertical. When we approximate the slope to be constant in the lines, the magnitude of the error due to elevation can be estimated. This is discussed more extensively in appendix B, where it is concluded that this error is not significant. This means that for this thesis, the elevation error will be disregarded.
To evaluate both the causal and acausal parts of the crosscorrelated panel, the range of slownesses evaluated contains both positive and negative values. The highest slowness value used is in principle determined by the minimum expected velocity with which the events propagated.

To also include panels that are dominated by air-wave arrivals and possibly other irregular noise, a very low value of 200 m/s is chosen. This gives a slowness of 0.005 s/m. The total evaluated range is therefore from -0.005 to 0.005 s/m. For a sufficient resolution in the Tau-P transform, 2400 linearly-spaced values are chosen within this range.
The same seismic events should reach all of the locations, so the specific station at which the analysis is done should not matter (Almagro Vidal et al., 2014). Therefore, the Tau-P transform is only evaluated with a single location as a virtual-source location. To get a location close to both lines, the station closest to the crossing of the two lines is chosen.

As a quality control of the Tau-P function, we can evaluate a synthetic trace containing two types of recorded events: four linear events and two hyperbolae are shown in the record in figure 4-4a. This test includes a full range of intercept values, not just $\tau = 0$.
According to the theory (Stein and Wysession, 2003), the linear events should show up as single points, while the hyperbolae become upward curving ellipses. As can be seen in figure 4-4b, this is roughly correct here. The hyperbolae become ellipses, but the linear events are more similar to stars, than points. This is expected due to the limited spatial extent of the array used for the evaluation of the Tau-P transform. The intercept times and slownesses associated with these stars are correct and the linear events could be reconstructed from this information.

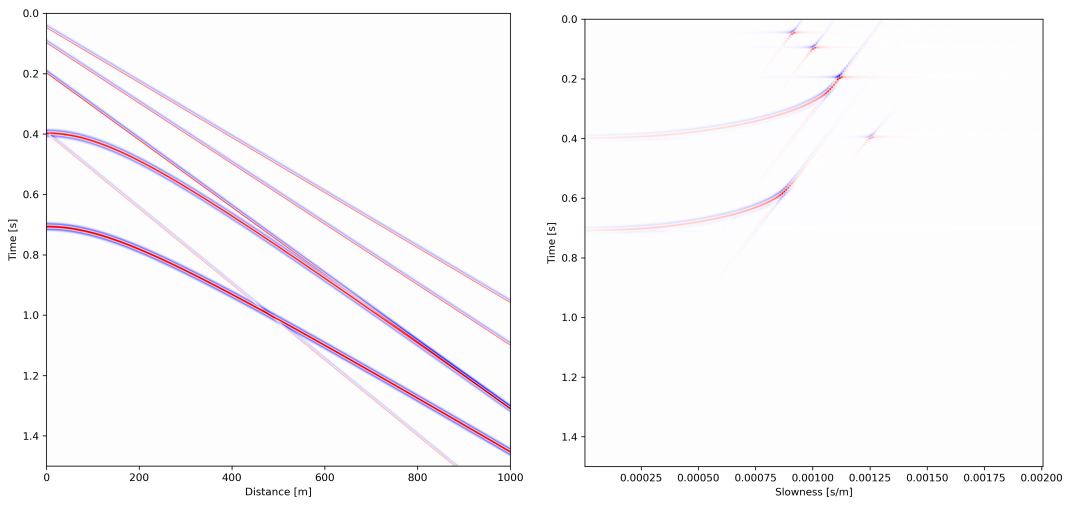

Figure 4-4: A synthetic seismic trace with various events and its Tau-P transform.
(a) Synthetic seismic record used for the test of the Tau-P function. Four linear events are recorded with velocities of 1100, 1000, 900 and 800 m/s. Two hyperbolas are recorded as reflected waves while propagating through media with velocities of 900 and 1100 m/s. All events use Ricker wavelets.
(b) Result of the Tau-P function applied to the synthetic record. The four linear events should show up as dots, but due to the limited spatial array are shown as small stars. The hyperbola turned into an ellipse as expected.

4-5 Autocorrelations

The autocorrelation process requires panels with events that have propagated close to vertically. This means that the selection criteria for the panels needs to be strict. Panels with a slowness of $|p < 0.0001\,\mathrm{s/m}|$ are used.
Different traces and panels can exhibit differences in the amplitudes of the event. This would mean that some traces or panels have a larger influence on the final stack than others. To remove this effect, each trace is normalised separately. The normalisation consists of dividing the trace by its Root Mean Square (RMS) value. Afterwards, each trace is autocorrelated, the causal part is isolated and added to a stack.
The stack is then filtered with a bandpass filter. The bandpass range is selected after visual inspection and a trial of different values. In the end, a Butterworth filter of order 4 with cut-off frequencies of 5 and 40 Hz is used. If we take this frequency band as the relevant one for the data, it can be applied to the data before the illumination analysis to obtain a new set of selected panels to improve the image.
The filtered stack is the final result, showing a virtual zero-offset reflection image.

4-6 Crosscorrelations

For the crosscorrelations, the panel-selection criterion can be relaxed, and includes more than only the vertically impinging events. This means that only the surface-wave-dominated events are to be removed. For this, panels are selected with a dominant slowness of $|p \leq 0.0002\,\mathrm{s/m}|$ (or a lower limit of 5,000 m/s).
Again, the traces in the selected panels are normalised by dividing each trace with its RMS value. Then, they are all crosscorrelated against a certain master trace. For the crosscorrelated section, the causal and acausal parts are not equal, meaning some thought should go into what part is used. The acausal part can be time-reversed and added to the causal part, but for locations where the illumination range is not well distributed, this would add noise to the data.
Ruigrok et al. (2010) use a different method, which they named Time Reversal Before Integration (TRBI) by them. An event arriving from one direction will be recorded at time zero at the virtual source location. It is found in negative times towards the direction it arrived from, while it can be found in positive times in the direction it is propagating in. Using the part from negative time and flipping it, effectively means that the event is used with a dip opposite to its original one. This balances the illumination and removes some noise.
We define positive distance as away from the base of each line (shown as a triangle in figure 2-4). Then, panels with a positive slowness use the acausal part at stations with a negative distance from the virtual-source position. The causal part is taken at stations with a positive distance from the virtual-source position. This is reversed for panels with a negative dominant slowness.
These corrected shot panels are then added to the stack for each virtual shot location. These shots are filtered with the same bandpass filter used for the autocorrelations. In the end, virtual common-shot gathers for each station are obtained.
A Wiener deconvolution is applied to the shot records to get rid of the source signature. The theory is slightly different, as the deconvolution assumes that the Green's function convolved

with the source wavelet yields the seismic record. For the SI case, the Green's function is convolved with the autocorrelated source function.
In mathematical terms this does not matter, as in both cases the desired time series is convolved with a shorter one, while the result is known. The method boosts lower and higher frequencies, so the bandpass filter is applied again afterwards.
The filtered shot gathers are then re-sorted into Common MidPoint (CMP) gathers based on the virtual-shot location. Every receiver location is also a virtual-shot location. This means that with a receiver spacing of roughly 20 m, the CMP spacing is 10 m. The receiver spacing can vary slightly from the regular spacing of 20 m. To mitigate this, CMPs which fall within 5 m from the 'ideal' midpoint location are binned together. The regular spacing means that the fold will increase towards the middle of the line, where it is equal to the number of receiver locations.
A very simple velocity model based on five velocity picks is used for Normal Move-Out (NMO) correction on the CMP gathers. Then, all of the traces in the gather are stacked together to obtain the final approximated zero-offset section.

Chapter 5

Results

5-1 Illumination analysis

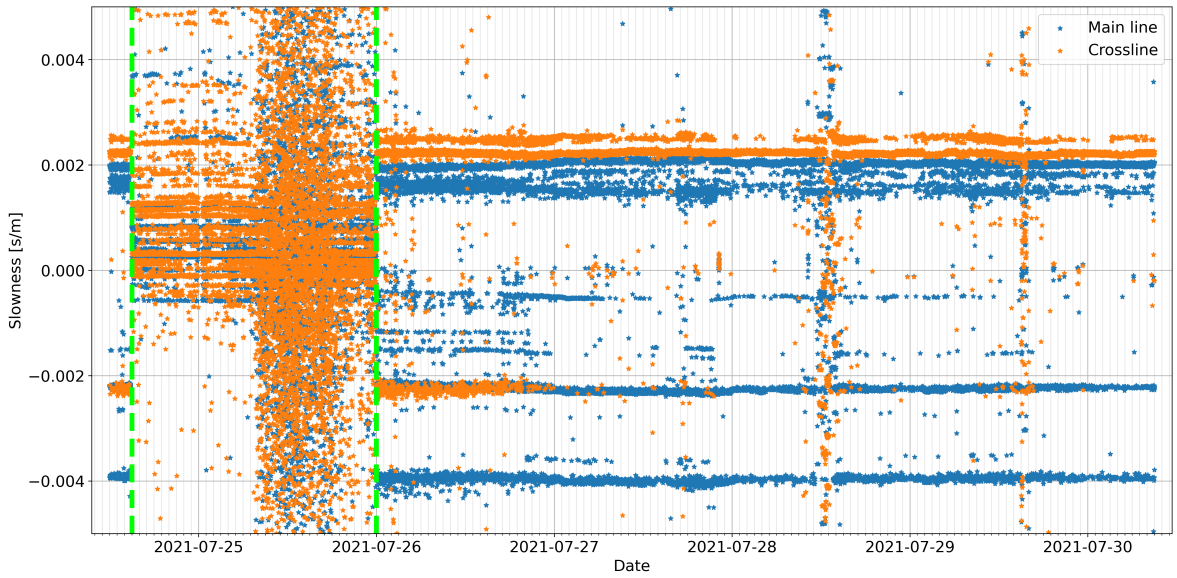

Figure 5-1: Results of the illumination analysis for the Z-component through time with the initial filter. Each star represents a recorded slowness on one of the lines (blue stars for the main line and orange stars for the cross line). The green vertical lines indicate a time range where the results show a higher variability and a break with the other results.

The results of the first illumination analysis through time can be seen in figure 5-1. This graph does not yet show how many panels are dominated by body-wave noise, but it does give a better insight into the general trend of the noise. The slowness must be close to zero for both lines for the dominant event to be a body wave. The short length of a single noise panel compared to the total length of the available data means that it is hard to distinguish which

stars belong to the same moment.
There are bands of slownesses that are roughly constant through time. For example, around -0.004 s/m for the main line or around 0.0023 s/m for the crossline. There are around five of these bands for the main line, while the crossline contains two. A third one is found around -0.0023 s/m for the crossline, but it stops at the start of the 27th of July.
These lines are not fully continuous, two prominent interruptions can be seen. The most obvious one is found between the vertical green lines (between 15:00 on the 24th and 00:00 on the 26th). In this zone, the trend that can be found during the rest of the recording time is fully broken. The data seems noisier, especially in the second half of the interval. Smaller horizontal lines of similar slownesses can still be found, but there are more and at different locations than before.
The second interruption of the larger lines around midday on the 28th and 29th. Here, there suddenly is a wider range of slownesses in the data. These only last for around four hours.

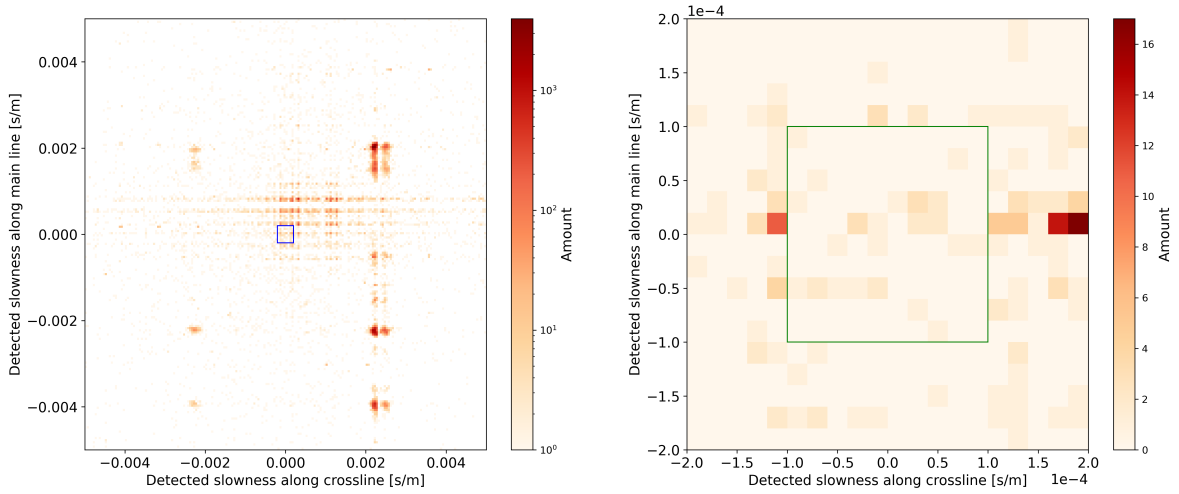

Figure 5-2: Two-dimensional histogram of the results of the illumination analysis. Left is the histogram of the full dataset. The blue square surrounds the panels used to create the crosscorrelations - all panels with a slowness below 0.0002 s/m for both lines. On the right is an enlarged version of this square. The green square indicates the panels used to create autocorrelations, with slownesses below 0.0001 s/m. Note that the color axes are not the same and the left one has logarithmic scaling.

A second way to look at the results is presented in figure 5-2. The relation between slowness and direction can be used as an indication of the direction events come from. It is immediately visible that only a very small amount of panels can be used for the crosscorrelations. Only 178 panels, or 0.35%, of the panels is used. For the autocorrelations, with an even stricter limitation, only 31 panels, or 0.061%, is used.
The plots also show that the majority of events are clustered together into peaks at certain combinations. The largest part is characterised by high, positive slownesses along the crossline and a range of slownesses along the main line. A smaller cloud of peaks is found towards positive values on both axes from the origin.
The selected panels show less grouping, possibly because the resolution is lower. There is one large peak around 0.0002 s/m crossline and 0 s/m main line. Looking back at the overview plot, this is part of one of the lines with peaks.

5-2 Autocorrelations

The zero-offset section along the main line, obtained by autocorrelating the data, can be seen in figure 5-3. The crossline equivalents of the following plots can be found in appendix A. The data is still very noisy, especially in some of the traces. However, there are some clearly coherent reflections to be recognised, for example, at 0.35 s TWT or 1.75 s TWT.

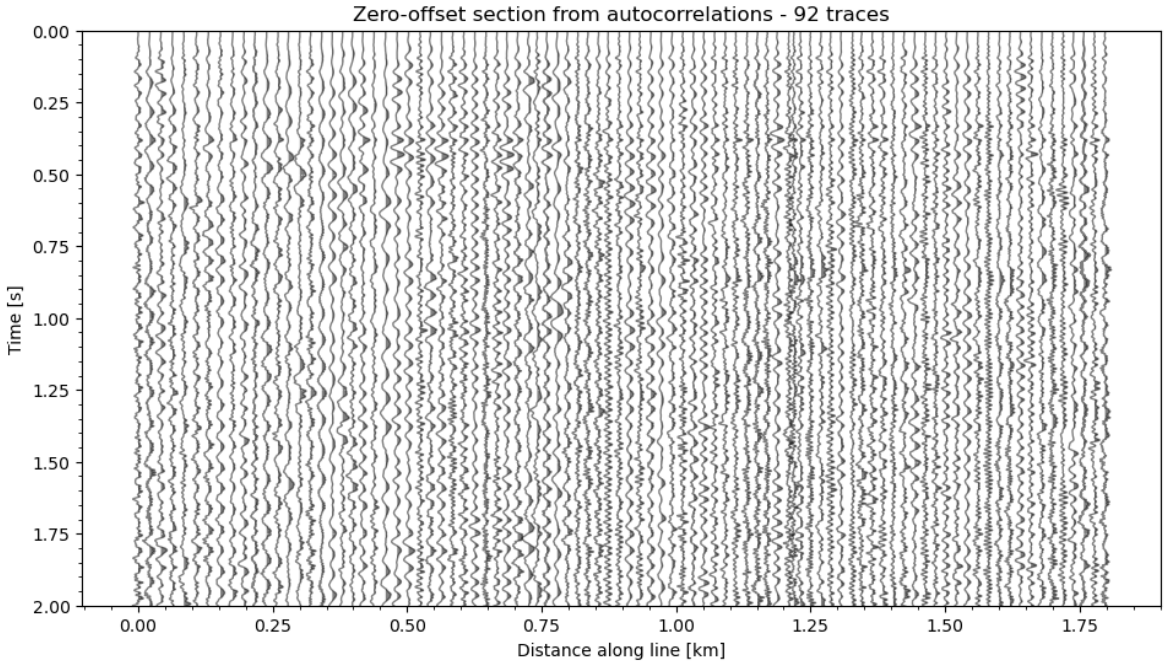

Figure 5-3: Zero-offset section based on autocorrelations. The earliest times are damped to remove the large autocorrelation spike at time zero. Afterwards, an automatic gain control function has been applied for the visualisation process.

To improve this image, a new manually designed filter is created. The best image was obtained using a Butterworth bandpass filter with a minimum cutoff frequency of 5 Hz and a maximum cutoff of 40 Hz. The new zero-offset section can be found in figure 5-4a. The bandpass filter has decreased the noise in the image, especially of high frequencies. More reflections can be recognised and they are more continuous. The peaks at reflections have become broader and are shifted to slightly higher time.

The new filter can also be applied to the data before the illumination analysis. This gives new results, shown in the next section. The resulting zero-offset section is shown in figure 5-4b. This is considered the final result retrieved by autocorrelating the noise panels. The full 10 s result is included in appendix A, where the other final sections can also be found in their full extent.
Although there is a definite improvement compared to figure 5-4a, the differences are minor. The most important change is that the reflections are more continuous.

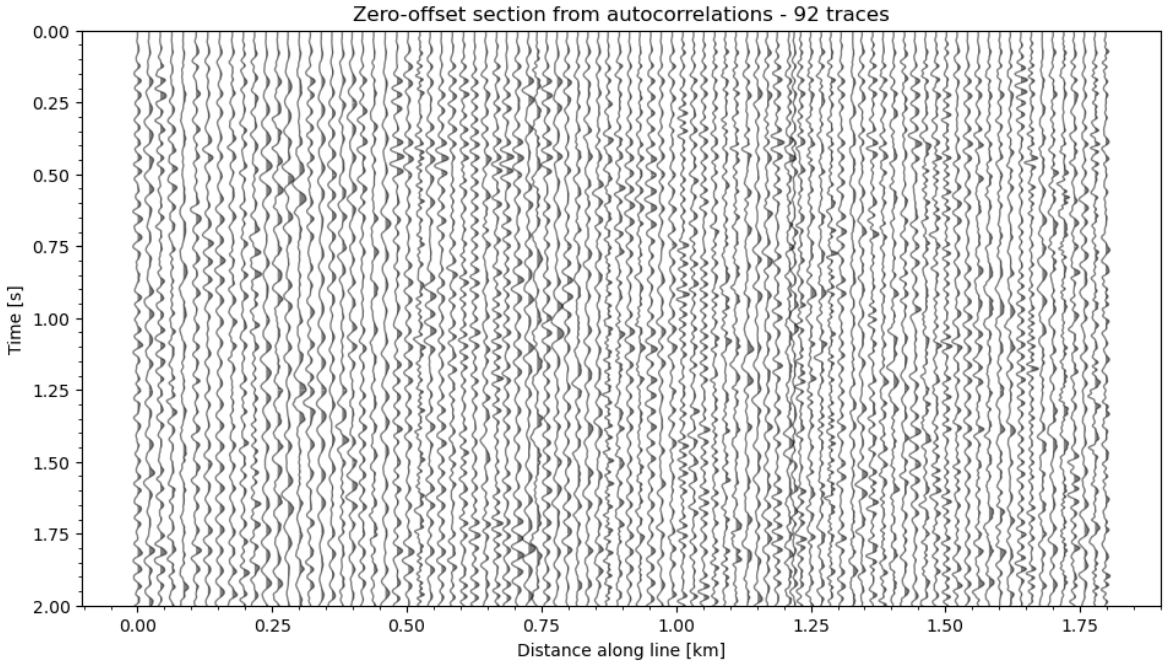

(a)

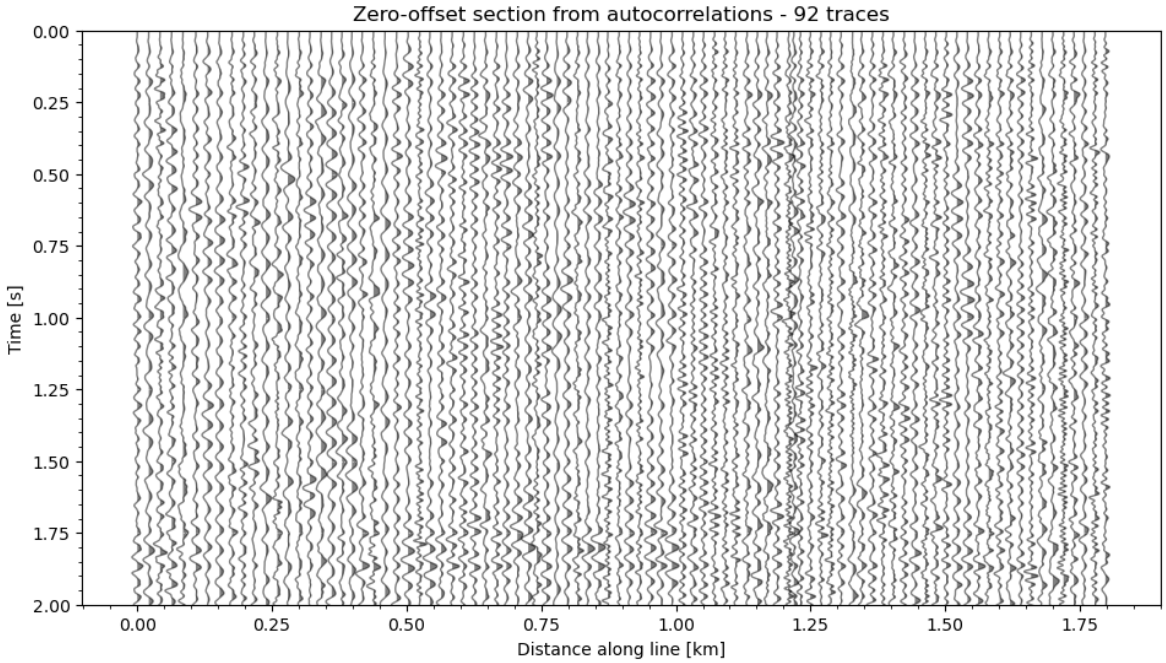

(b)

Figure 5-4: **(a)** The same section as in figure 5-3 with the same plotting parameters. Now a bandpass filter between 5 and 40 Hz has been applied. Noise has been reduced and reflections are generally more clearly visible.
(b) The autocorrelated zero-offset section based on the newly selected noise panels. The image processing is the same as in figure 5-4a. Image quality has slightly improved.

5-3 A new filter

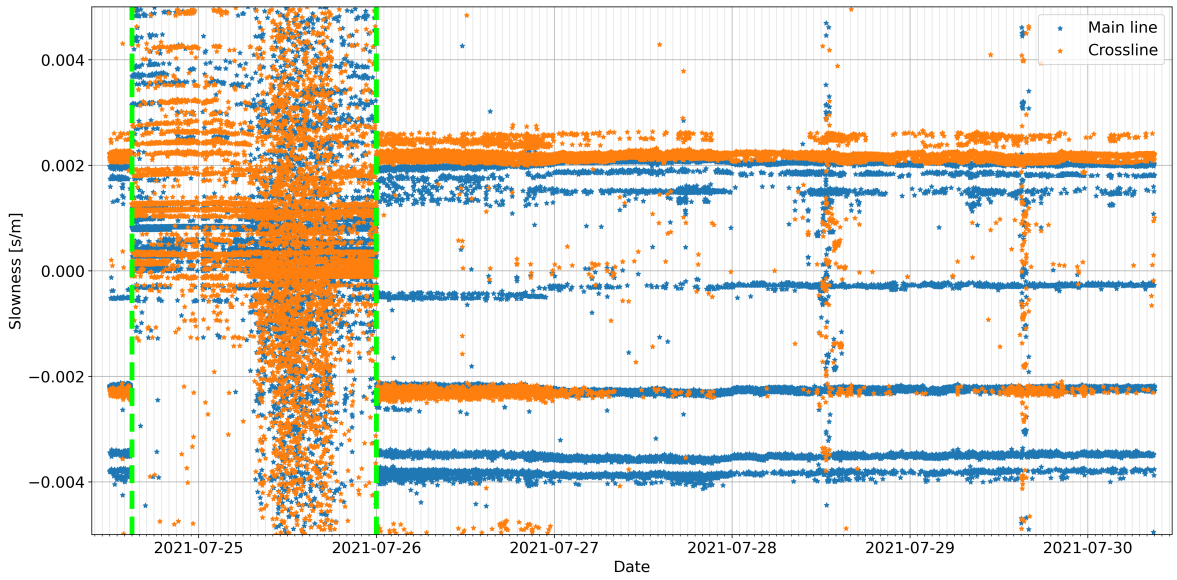

Figure 5-5: The results of the second illumination analysis. A bandpass filter between 5 and 40 Hz has been applied before crosscorrelation. The plotting routine is the same as in figure 5-1. The general characteristics are the same, but the lines mentioned in figure 5-1 are clearer.

The results of the illumination analysis with the new filter can be found in figures 5-5 and 5-6. The illumination results through time show generally the same trend as before. However, the slownesses are clustered together more. Especially the large lines at 0.0020 s/m or -0.0023 s/m are more constant and continuous.
The same break between the vertical, green lines is still there. Even though, the zone is still chaotic, the new filter has the same result. The spread of values is smaller and the horizontal lines in the data are more prominent.
The histogram in figure 5-6 shows that the illumination is spread slightly more evenly. The clusters of similar slownesses are still visible, but the peaks are lower. Although the distribution of the panels has changed, the amount of panels that can be used for both the auto- and crosscorrelations remains roughly the same. The amount of panels available for the autocorrelations has increased to 36, while the amount available for the crosscorrelations has decreased to 146.
As the filter decreased the noise levels in both the zero-offset section and the results of the illumination analysis, it is assumed that the second analysis is more accurate. The panels that are selected with the first filter, but not with the second, are selected incorrectly. Thus, further processing uses the second filter.

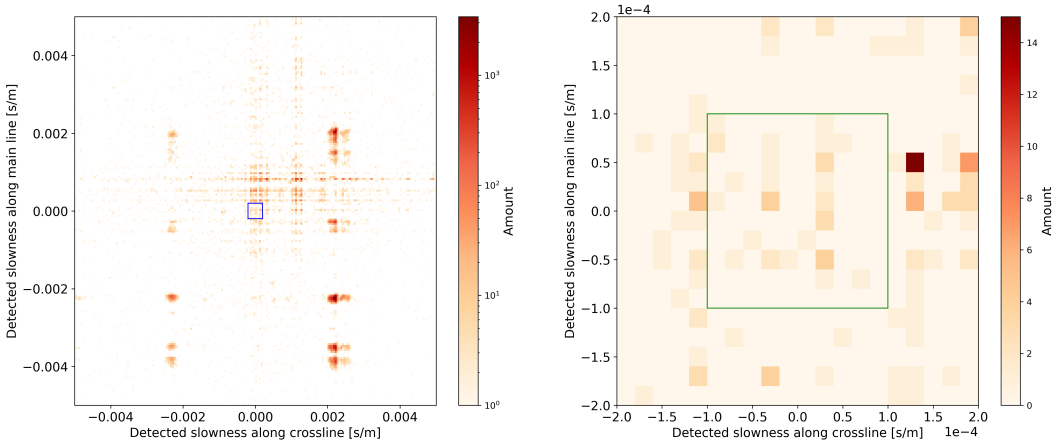

Figure 5-6: The results of the second illumination analysis. Here, a bandpass filter between 5 and 40 Hz has been applied before crosscorrelation. The plotting routine is the same as in figure 5-2. The image shows a slightly more spread illumination.

5-4 Crosscorrelations

An example of a virtual shot record, the result of crosscorrelating the noise panels, can be seen in figure 5-7a. In the image, top muting has been applied based on a linear move-out. This removes non-reflected energy, such as refracted arrivals, from the section. The shot itself looks noisy and hyperbolae are difficult to detect. They do present as roughly horizontal lines at for example 0.85 or 1.75 s TWT. Interestingly, these lines move slightly up and down through time, which should physically not be possible. This indicates something about the quality of the data.

The same can be seen in the CMP gathers, shown in figure 5-7b. The hyperbola are even more difficult to trace here. A second complication is that because of the small offsets in the section, the hyperbola do not show significant time differences. This makes the velocity analysis more difficult, as the results are more ambiguous. The final velocity model is based on the velocity picks and the laboratory work from Janssen et al. (2022). The picks are shown in figure 5-7b and in table 5-1. The values between the picks are linearly interpolated.

The final section that results from the NMO correction and stacking is shown in figure 5-8. The section shows lower frequency reflections compared to the result from the autocorrelations. The reflections are more clearly visible, though. Comparing the two different sections, the major reflections that can be found in one section, can also be found in the other.

Time [s]	Velocity [m/s]
0.0	1800
0.35	2200
0.5	2500
1.1	4000
2.0	6000

Table 5-1: Velocity picks used to create velocity model for NMO correction. Values between these have been linearly interpolated.

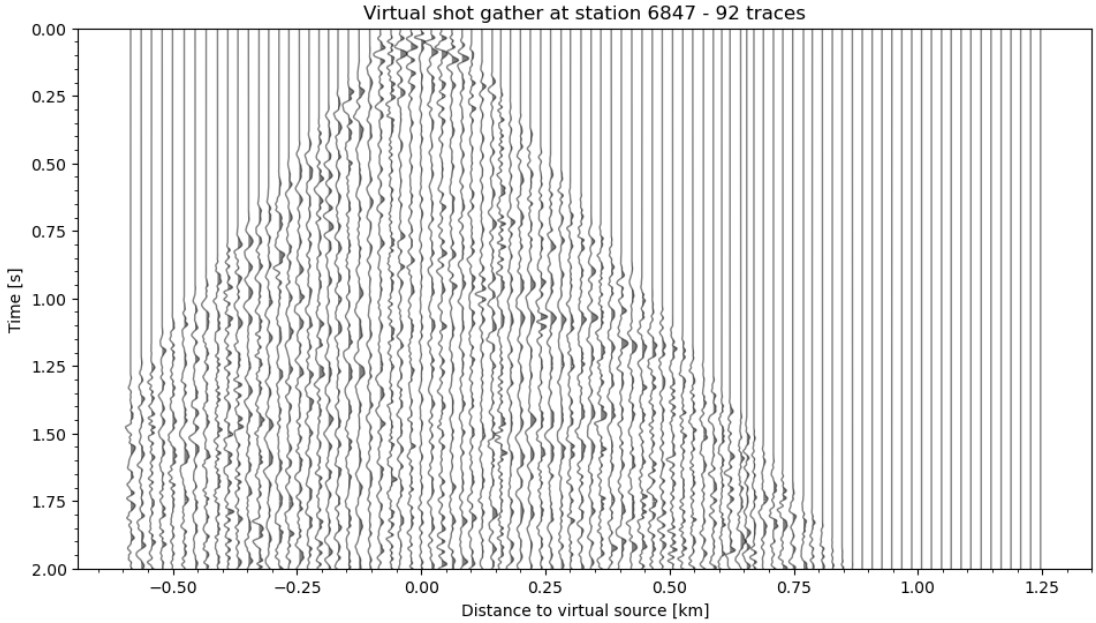

(a)

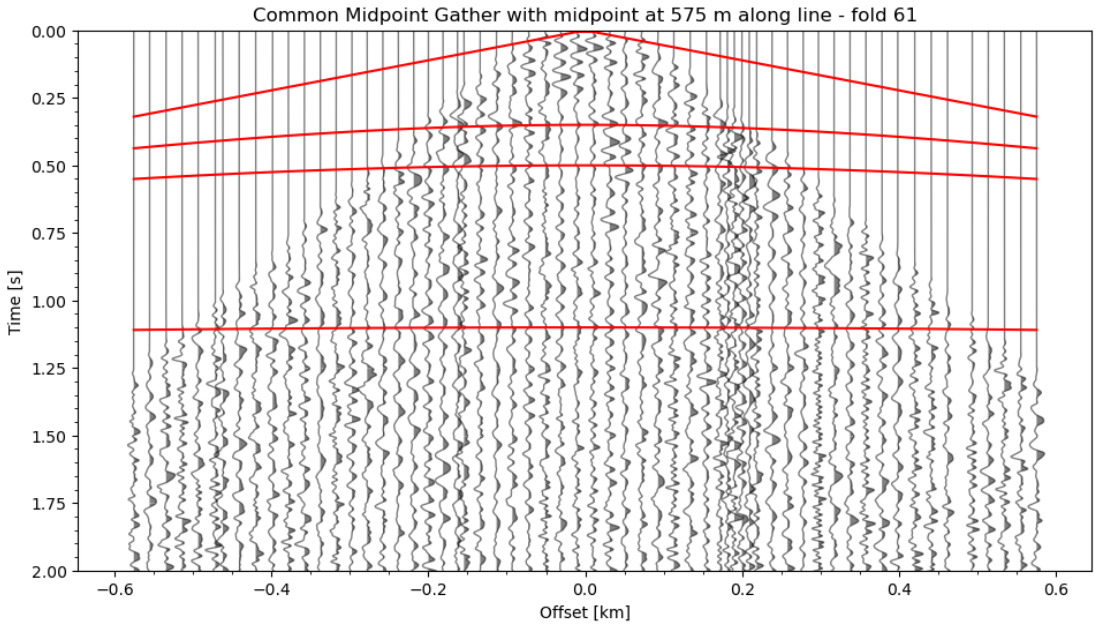

(b)

Figure 5-7: **(a)** Common-source gather obtained from crosscorrelating and stacking noise data. Afterwards, a Wiener deconvolution has been applied. Then automatic gain control and muting are applied to make the plot better interpretable. The muting is implemented by multiplying each trace with a ramp function that goes from 0 to 1 in 0.1 s. The start of the ramp is determined by a linear move-out of 400 m/s that is shifted by 0.15 s back in time.
(b) Common-midpoint gather created by resorting the common-source gathers. The selected midpoint is close to the virtual source position of figure 5-7a. Again, automatic gain control and muting are applied for plotting purposes. The red lines indicate the hyperbolae used in the velocity analysis - each one indicates a velocity pick. For the exact values, see table 5-1.

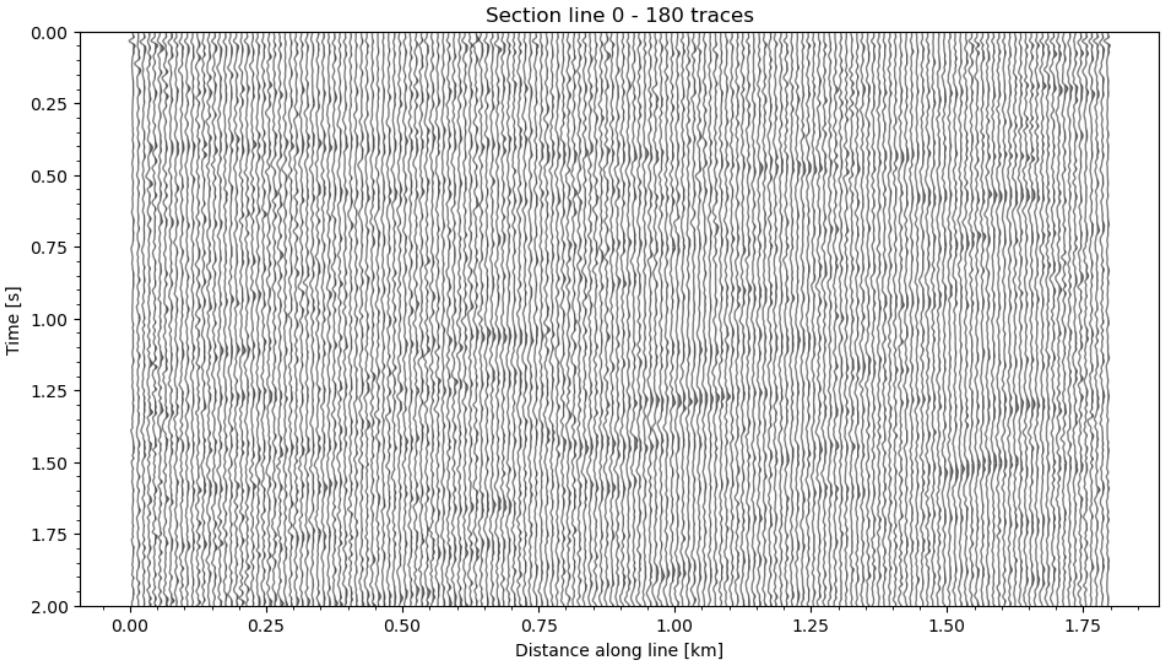

Figure 5-8: The stacked section that results from stacking the CMP gathers after NMO correction with the velocity picks in table 5-1. Equivalent for the cross line can be found as figure A-4.

Chapter 6

Discussion

6-1 Illumination analysis

The illumination analysis shows that most of the recorded events are caused by a few continually active noise sources. These appear as horizontal lines in the time plots. The same is shown in the histograms, where specific combinations of slowness values show large peaks at high slownesses.
As most of the large peaks have a high, positive slowness along the cross line, most of the events originate from east of the line. These noise sources are likely surface wave noise from activities around the geothermal power plant.
The large break on the 24th and 25th of July correlates with the large storm that passed over the field area. It could be that the storm was strong enough to overpower all other noise sources during this time. The sharp breaks in different dominant events are also made worse by the time scale - a transition of 30 minutes is still sudden on the scale used in the plots. Although it is not fully convincing, it is the best explanation for the sudden switch in noise sources.
The vertical lines that can be found on the 28th and 29th are caused by the active-source campaign. It is no surprise that the increased anthropogenic activity along the line and the vibrator source moving along the line introduced new noise sources.
The amount of noise panels that can be used is low with only 0.35% and 0.061% percent being available for the crosscorrelations and autocorrelations, respectively. It would be worthwhile to repeat the illumination analysis with overlap in the noise panels to find more body-wave dominated panels without decreasing the panel size. Though, this would also increase the computation time, which is already significant. A suggestion would be to have an overlap of 7.5 s.
The bandpass range found for the second filter is no surprise, looking back at the frequency spectrum of a local seismic event that was used as an example in figure 4-2 - the majority of the energy is found exactly within this range.
The filter removes noise from the data, such that the slowness can be determined more accurately. This meant that the slowness through time is also less chaotic. It does not necessarily provide new insights into the noise sources, but they have become clearer in the data.

6-2 Zero-offset sections

It is somewhat difficult to compare the two types of sections. The autocorrelations have created noisier sections that contain sharper reflectors. Whereas the sections from crosscorrelations are of a lower-frequency content, but exhibit more continuous reflectors. As the reflection hyperbolae in the CMP gather were wavy. The stacking has smeared out these reflections, resulting in the lower-frequency content.
It seems that most reflectors that can be found on the autocorrelation sections, can also be found on the crosscorrelation sections. Sometimes the location does not align perfectly. Because there are a multitude of reflections to be found, it is possible that these reflections line up accidentally, rather than because they are the same.
Intrepreted sections based on both lines are shown in figure 6-1. On this figure, the reflectors are also indicated. Large continuous reflectors can be traced on all sections, both on the main line and the cross line, at 0.06, 0.2, 0.4 and around 1.75 s. The reflections found in the autocorrelations are almost always horizontal and flat. The reflections from the crosscorrelations are less well-defined, slightly vertically waving through the section. Up to about 0.5 s, the reflections are mostly horizontal. At times later than 0.5 s, the reflections begin to dip towards the south on the main line and towards the west on the crossline.
The reflections that are only found on the stacked section are generally dipping reflectors that often connect horizontal reflectors found on both sections. As mentioned during the theory, the method creating the zero-offset section has problems imaging dipping reflectors. Consequently, the dipping reflectors are only found on the stacked section.
In general, the sections show a horizontally layered subsurface with some layers that pinch out towards the south. The reflection at 1.75 s could be the base of the Hengill volcano. The layers that pinch out could be lava flows coming from the main Hengill volcano towards the north.
The other data collected during the survey is not yet fully processed, meaning the results can only be compared with the geological sections.

The data processing could be repeated with a different illumination analysis scheme. Different beamforming methods are used in the literature (see also Hassing (2022)). This could provide more panels for further processing. A second option to improve the quality of the results is to expand the processing of the virtual shot gathers. More advanced seismic reflection processing methods can be applied, such as statics corrections or post-stack image enhancements.
Because the current dataset contains the active-source survey, active-source seismic interferometry (Balestrini et al., 2020, Plescia et al., 2022) can be performed and compared with the current results. Similarly, the data recorded on the DAS cable can be processed with the results of the illumination analysis of this thesis. This would give a comparison with different imaging methods.
To get more information on the effects of the CO_2 injection, more surveys over time could reveal differences in the seismic sections. The current results only show a snapshot at a time after injection has started. Ideally, data from before injection should also be available, but as mineralisation happens in the reservoir, there should be visible differences over time.

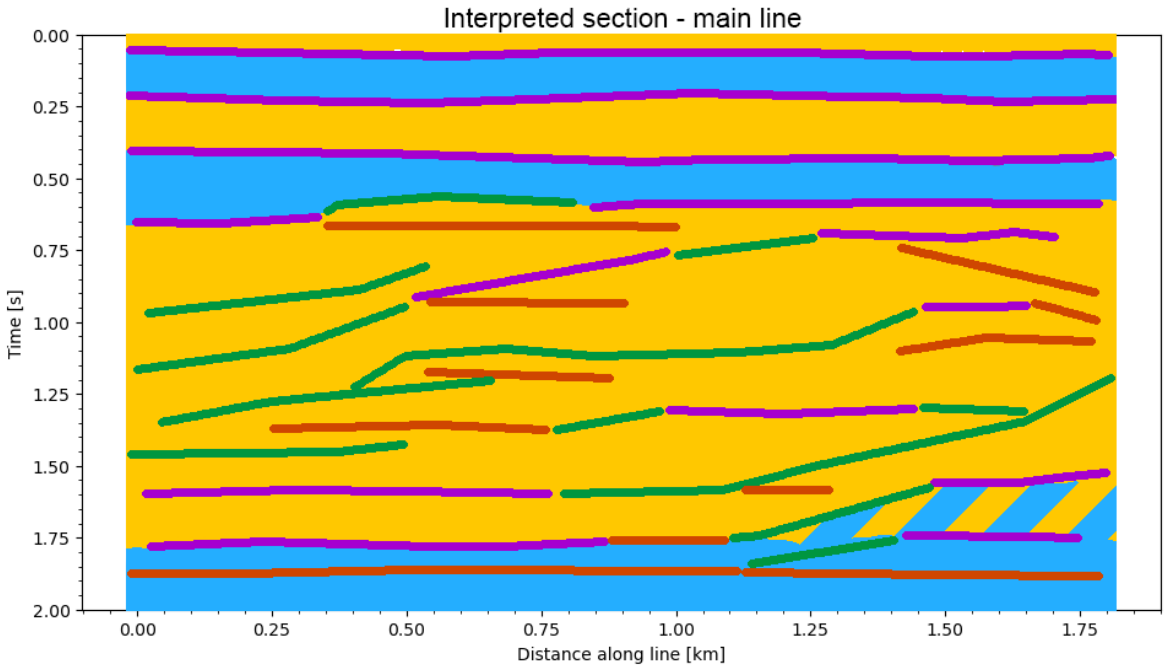

(a)

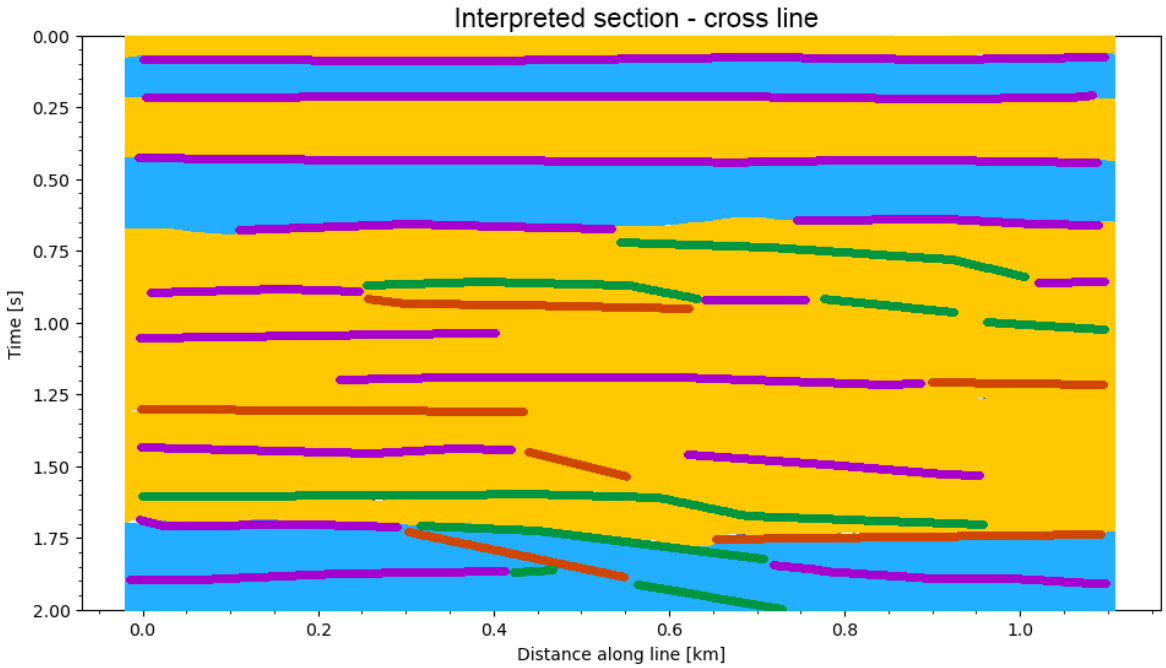

(b)

Figure 6-1: Interpreted sections of the main **(a)** and cross **(b)** line. Lines indicate reflectors from the final sections.
The purple lines show where the two types of sections agree. Orange lines show reflectors that were only identified on the zero-offset sections, while green lines indicate reflectors that were only identified on the stacked sections.
Background colours are kept the same as the geological section in figure 2-2. Blue indicates lava sequences and yellow indicates hyaloclastites. The striped zone indicates an uncertain zone.

Chapter 7

Conclusion

In July, 2021, both passive and active seismic data were collected near the Hellisheiði geothermal power plant in Iceland. The aim of this survey is to develop seismic monitoring methods for reinjection of CO_2. For this reason, the data is processed with various seismic methods. In this thesis, seismic interferometry (SI) is applied to the passive seismic data. As this data is only available in 2021, it is only used for imaging.

An illumination analysis is performed to distinguish noise panels dominated by surface-wave noise from ones dominated by body-wave noise. It showed that only a small part of the panels could be used for SI. It also showed that the noise originates from a few types of noise sources that are continually active.

The noise panels were processed to obtain an image of the subsurface in time in two different ways. First by autocorrelating selected panels, second by crosscorrelating to obtain virtual shot records. The zero-offset sections from autocorrelations exhibit higher-frequency, horizontal reflectors, but appear noisier. The autocorrelation method also has difficulty imaging dipping reflectors. The stacked sections from crosscorrelations exhibit lower-frequency reflectors that are slightly bumpy. The two methods provide complementary information.

Together, interpreted sections are created. Multiple reflectors are found that correlate between the two sections. The basic geology of the area is reflected in the interpreted section. The sections show horizontal layers of hyaloclastites and lava sequences down to 0.5 s TWT. Below this, reflectors dip towards the south. The base of the Hengill volcano is found at 1.75 s TWT.

Bibliography

Alfredsson, H. A., Oelkers, E. H., Hardarsson, B. S., Franzson, H., Gunnlaugsson, E., & Gislason, S. R. (2013). The geology and water chemistry of the Hellisheidi, SW-Iceland carbon storage site. *International Journal of Greenhouse Gas Control*, *12*, 399–418. https://doi.org/10.1016/j.ijggc.2012.11.019

Almagro Vidal, C., Draganov, D., Van der Neut, J., Drijkoningen, G., & Wapenaar, K. (2014). Retrieval of reflections from ambient noise using illumination diagnosis. *Geophysical Journal International*, *198*(3), 1572–1584. https://doi.org/10.1093/gji/ggu164

Aradóttir, E., Gunnarsson, I., Sigfússon, B., Gislason, S., Oelkers, E., Stute, M., Matter, J., Snaebjörnsdottir, S. Ó., Mesfin, K. G., Alfredsson, H. A., Hall, J., Arnarsson, M. T., Dideriksen, K., Júliusson, B. M., Broecker, W. S., & Gunnlaugsson, E. (2015). Towards cleaner geothermal energy: Subsurface sequestration of sour gas emissions from geothermal power plants.

Ármannsson, H., Fridriksson, T., & Kristjánsson, B. R. (2005). Co2 emissions from geothermal power plants and natural geothermal activity in iceland. *Geothermics*, *34*(3), 286–296. https://doi.org/10.1016/j.geothermics.2004.11.005

Aster, R., McNamara, D., & Bromirski, P. (2010). Global trends in extremal microseism intensity. *Geophysical Research Letters*, *37*(L14303). https://doi.org/10.1029/2010GL043472

Balestrini, F., Sacchi, M., Malehmir, A., Marsden, P., Ghose, R., & Draganov, D. (2020). Data reconstruction using seismic interferometry applied to active-source data from the ludvika mines of sweden. *NSG2020 3rd Conference on Geophysics for Mineral Exploration and Mining*, *2020*(1), 1–5.

Benson, S. M., & Cole, D. R. (2008). CO_2 sequestration in deep sedimentary formations. *Elements*, *4*, 325–331. https://doi.org/10.2113/gselements.4.5.325

Bertani, R., & Thain, I. (2002). Geothermal power generating plant CO_2 emission survey. *IGA News*, *49*, 1–3.

Beyreuther, M., Barsch, R., Krischer, L., Megies, T., Behr, Y., & Wassermann, J. (2010). ObsPy: A Python toolbox for seismology. *Seismological Research Letters*, *81*(3), 530–533.

Boullenger, B., Verdel, A., Paap, B., Thorbecke, J., & Draganov, D. (2015). Studying CO_2 storage with ambient-noise seismic interferometry: A combined numerical feasibility study and field-data example for Ketzin, Germany. *Geophysics*, *80*(1), Q1–Q13. https://doi.org/10.1190/GEO2014-0181.1

Carbfix. (n.d.). *Our Story*. Retrieved August 1, 2022, from https://www.carbfix.com/our-story

Draganov, D., & Ruigrok, E. (2014). Passive seismic interferometry for subsurface imaging. In M. Beer, I. A. Kougioumtzoglou, E. Patelli, & I. S.-K. Au (Eds.), *Encyclopedia of earthquake engineering* (pp. 1–13). Springer Berlin Heidelberg. https://doi.org/10.1007/978-3-642-36197-5_378-1

Duran Neme, J. A. (2021). *Numerical sensitivity kernels in elastic media for imaging purposes and seismic tomography in the hengill geothermal field* (Doctoral dissertation). ETH Zurich.

Durucan, S., Korre, A., Parlaktuna, M., Senturk, E., Wolf, K.-H., Chalari, A., Stork, A., Nikolov, S., de Kunder, R., Sigfusson, B., Hjörleifsdóttir, V., Andersen, N., & Poletto, F. (2021). SUCCEED: A CO_2 storage and utilisation project aimed at mitigating against greenhouse gas emissions from geothermal power production. https://doi.org/10.2139/ssrn.3819789

Einarsson, P. (2008). Plate boundaries, rifts and transforms in iceland. *Jökull*, *58*(12), 35–58.

Franzson, H., Gunnlaugsson, E., Árnason, K., Sæmundsson, K., Steingrímsson, B., & Harðarson, B. (2010). The Hengill goethermal system, conceptual model and thermal evolution.

Franzson, H., Kristjánsson, B., Gunnarsson, G., Björnsson, G., Hjartarson, A., Steingrimsson, B., Gunnlaugsson, E., & Gislason, G. (2005). The Hengill-Hellisheidi geothermal field. Development of a conceptual geothermal model, 3916–3926. https://doi.org/10.1016/j.egypro.2017.03.1523

Fridriksson, T., Merino, A. M., Orucu, A. Y., & Audinet, P. (2017). Greenhouse gas emissions from geothermal power production. *Proc 42nd Workshop on Geothermal Reservoir Eng Stanford University February*, 13–15.

Gebrehiwot, K., Koestono, H., Franzson, H., & Mortensen, A. K. (2010). Borehole geology and hydrothermal alteration of well HE-24, Hellisheidi geothermal field, SW-Iceland. *Proceedings World Geothermal Congress*. https://doi.org/10.1.1.1079.373

Gislason, S. R., Wolff-Boenisch, D., Stefansson, A., Oelkers, E. H., Gunnlaugsson, E., Sigurdardottir, H., Sigfusson, B., Broecker, W. S., Matter, J. M., Stute, M., Axelsson, G., & Fridriksson, T. (2010). Mineral sequestration of carbon dioxide in basalt: A pre-injection overview of the CarbFix project. *International Journal of Greenhouse Gas Control*, *4*, 537–545. https://doi.org/10.1016/j.ijggc.2009.11.013

Gualtieri, L., Stutzmann, E., Capdeville, Y., Ardhuin, F., Schimmel, M., Mangeney, A., & Morelli, A. (2013). Modelling secondary microseismic noise by normal mode summation. *Geophysical Journal International*, *193*(3), 1732–1745. https://doi.org/10.1093/gji/ggt090

Gunnarsson, I., Aradòttir, E. S., Oelkers, E. H., Clark, D. E., Arnarson, M. þ., Sigfússon, B., Snæbjörnsdòttir, S. Ó., Matter, J. M., Stute, M., Jùlíusson, B. M., et al. (2018). The rapid and cost-effective capture and subsurface mineral storage of carbon and sulfur at the CarbFix2 site. *International Journal of Greenhouse Gas Control*, *79*, 117–126. https://doi.org/10.1016/j.ijggc.2018.08.014

Hardarson, B. S., Einarsson, G. M., Kristjánsson, B. R., Gunnarsson, G., Helgadóttir, H. M., Franzson, H., Árnason, K., Ágústsson, K., & Gunnlaugsson, E. (2010). Geothermal

reinjection at the Hengill triple junction, SW Iceland. *Proceedings World Geothermal Congress, Bali, Indonesia*, 25–29.

Hassing, S. (2022). Overview of the applicability of different seismic interferometry sources to monitor CO_2 after reinjection. *Research Module*, 1–12.

Helgadóttir, H. M., Snaebjörnsdottir, S., Níelsson, S., Gunnarsdóttir, S. H., Matthíasdóttir, T., Hardarson, B., Einarsson, G. M., & Franzson, H. (2010). Geology and hydrothermal alteration in the reservoir of the hellisheidi high temperature system, sw-iceland. *Proceedings, World Geothermal Congress, Bali, Indonesia*, 25–29.

IPCC. (2005). *IPCC special report on carbon dioxide capture and storage*. Cambridge University Press.

IPCC. (2018). Global warming of 1.5 C. An IPCC Special Report on the impacts of global warming of 1.5°C above pre-industrial levels and related global greenhouse gas emission pathways, in the context of strengthening the global response to the threat of climate change, sustainable development, and efforts to eradicate poverty. *[Masson-Delmotte, Valérie and Zhai, Panmao and Pörtner, Hans-Otto and Roberts, Debra and Skea, Jim and Shukla, Priyadarshi R and Pirani, Anna and Moufouma-Okia, W and Péan, C and Pidcock, R and others]*.

Jakobsdóttir, S. S. (2008). Seismicity in iceland: 1994–2007. *Jökull*, *58*, 75–100.

Janssen, M., Draganov, D., Bos, J., Farina, B., Barnhoorn, A., Poletto, F., van Otten, G., Wolf, K., & Durucan, S. (2022). Monitoring CO2 Injection into Basaltic Reservoir Formations at the Hellisheiði Geothermal Site in Iceland: Laboratory Experiments. *83rd EAGE Annual Conference & Exhibition*, *2022*(1), 1–5.

Kappus, M. E., Harding, A. J., & Orcutt, J. A. (1990). A comparison of Tau-P transform methods. *Geophysics*, *55*(9), 1202–1215. https://doi.org/10.1190/1.1442936

Krischer, L., Megies, T., Barsch, R., Beyreuther, M., Lecocq, T., Caudron, C., & Wassermann, J. (2015). ObsPy: A bridge for seismology into the scientific Python ecosystem. *Computational Science & Discovery*, *8*(1), 014003.

Matter, J., Broecker, W., Gislason, S., Gunnlaugsson, E., Oelkers, E., Stute, M., Sigurdardóttir, H., Stefansson, A., Alfreðsson, H., Aradóttir, E., et al. (2011). The CarbFix pilot project – storing carbon dioxide in basalt. *Energy Procedia*, *4*, 5579–5585. https://doi.org/10.1016/j.egypro.2011.02.546

Matter, J., Stute, M., Snaebjörnsdottir, S., Oelkers, E., Gislason, S., Aradottir, E., Sigfusson, B., Gunnarsson, I., Sigurdardottir, H., Gunnlaugsson, E., et al. (2016). Rapid carbon mineralization for permanent disposal of anthropogenic carbon dioxide emissions. *Science*, *352*(6291), 1312–1314. https://doi.org/10.1126/science.aad8132

Oelkers, E. H., & Cole, D. R. (2008). Carbon dioxide sequestration a solution to a global problem. *Elements*, *4*(5), 305–310. https://doi.org/10.2113/gselements.4.5.305

ON Power. (n.d.). *Our power plants*. Retrieved May 20, 2022, from https://www.on.is/en/about-us/power-plants/

Oren, C., & Nowack, R. L. (2016). Seismic body-wave interferometry using noise autocorrelations for crustal structure. *Geophysical Journal International*, ggw394. https://doi.org/10.1093/gji/ggw394

O'Sullivan, M., Gravatt, M., Popineau, J., O'Sullivan, J., Mannington, W., & McDowell, J. (2021). Carbon dioxide emissions from geothermal power plants. *Renewable Energy*, *175*, 990–1000. https://doi.org/10.1016/j.renene.2021.05.021

Panea, I., Draganov, D., Almagro Vidal, C., & Mocanu, V. (2014). Retrieval of reflections from ambient noise recorded in the Mizil area, Romania. *Geophysics*, *79*(3), Q31–Q42. https://doi.org/10.1190/GEO2013-0292.1

Plescia, S. M., Sheehan, A. F., & Haines, S. S. (2022). Active-source interferometry in marine and terrestrial environments: Importance of directionality and stationary phase. *Bulletin of the Seismological Society of America*, *112*(2), 634–645.

Polychronopoulou, K., Lois, A., & Draganov, D. (2020). Body-wave passive seismic interferometry revisited: mining exploration using the body waves of local microearthquakes. *Geophysical prospecting*, *68*, 232–253. https://doi.org/10.1111/1365-2478.12884

Ratouis, T. M., Snæbjörnsdóttir, S. O., Gunnarsson, G., Gunnarsson, I., Kristjánsson, B. R., & Aradóttir, E. S. (2019). Modelling the complex structural features controlling fluid flow at the CarbFix2 reinjection site, Hellisheiði geothermal power plant, SW-Iceland. *Proceeding: 44th Workshop on Geothermal Reservoir Engineering, Stanford University, CA, USA*.

Ratouis, T. M., Snæbjörnsdóttir, S. Ó., Voigt, M. J., Sigfússon, B., Gunnarsson, G., Aradóttir, E. S., & Hjörleifsdóttir, V. (2022). Carbfix 2: A transport model of long-term co2 and h2s injection into basaltic rocks at hellisheidi, sw-iceland. *International Journal of Greenhouse Gas Control*, *114*, 103586.

Ruigrok, E., Campman, X., Draganov, D., & Wapenaar, K. (2010). High-resolution lithospheric imaging with seismic interferometry. *Geophysical Journal International*, *183*(1), 339–357.

Sigfússon, B., Arnarson, M. þ., Snæbjörnsdóttir, S. Ó., Karlsdóttir, M. R., Aradóttir, E. S., & Gunnarsson, I. (2018). Reducing emissions of carbon dioxide and hydrogen sulphide at Hellisheidi power plant in 2014-2017 and the role of CarbFix in achieving the 2040 Iceland climate goals. *Energy Procedia*, *146*, 135–145. https://doi.org/10.1016/j.egypro.2018.07.018

Sigfússon, B., Gislason, S. R., Matter, J. M., Stute, M., Gunnlaugsson, E., Gunnarsson, I., Aradottir, E. S., Sigurdardottir, H., Mesfin, K., Alfredsson, H. A., Wolff-Boensich, D., Arnarsson, M. T., & Oelkers, E. H. (2015). Solving the carbon-dioxide buoyancy challenge: The design and field testing of a dissolved CO_2 injection system. *International Journal of Greenhouse Gas Control*, *37*, 213–219. https://doi.org/10.1016/j.ijggc.2015.02.022

Snæbjörnsdóttir, S. Ó., Tómasdóttir, S., Sigfússon, B., Aradóttir, E. S., Gunnarsson, G., Niemi, A., Basirat, F., Dessirier, B., Gislason, S. R., Oelkers, E. H., et al. (2018). The geology and hydrology of the CarbFix2 site, SW-Iceland. *Energy Procedia*, *146*, 146–157. https://doi.org/10.1016/j.egypro.2018.07.019

Snæbjörnsdóttir, S. Ó., Wiese, F., Fridriksson, T., Ármansson, H., Einarsson, G. M., & Gislason, S. R. (2014). Co2 storage potential of basaltic rocks in iceland and the oceanic ridges. *Energy Procedia*, *63*, 4585–4600.

Snieder, R. (2004). Extracting the Green's function from the correlation of coda waves: A derivation based on stationary phase. *Physical Review*, *69*(046610), 1–8. https://doi.org/10.1103/PhysRevE.69.046610

Stein, S., & Wysession, M. (2003). *An introduction to seismology, earthquakes and earth structure*. Blackwell Publishing.

USGS. (n.d.). *M 8.2 - 99 km SE of Perryville, Alaska*. Retrieved May 13, 2022, from https://earthquake.usgs.gov/earthquakes/eventpage/ak0219neiszm/executive

VolcanoDiscovery. (n.d.). *Past earthquakes in iceland: Jul 23-31, 2021 - list, stats and map.* Retrieved May 13, 2022, from https://www.volcanodiscovery.com/earthquakes/iceland/archive/2021-07-23-2021-07-31.html

Wapenaar, K., Draganov, D., Snieder, R., Campman, X., & Verdel, A. (2010). Tutorial on seismic interferometry: Part 1 - basic principles and applications. *Geophysics*, *75*(5), 195–209. https://doi.org/10.1190/1.3457445

Wapenaar, K., & Fokkema, J. (2006). Green's functions representations for seismic interferometry. *Geophysics*, *71*(4), 33–46. https://doi.org/10.1190/1.2213955

Wu, Y., & Li, P. (2020). The potential of coupled carbon storage and geothermal extraction in a co 2-enhanced geothermal system: A review. *Geothermal Energy*, *8*(1), 1–28. https://doi.org/10.1186/s40517-020-00173-w

Appendix A

Extra sections

This appendix contains extra figures that were not included in the main text. They are good to include for the results, but break the text too much to include earlier.

A-1 Cross line sections

These sections are the cross line equivalents of the figures shown in the results.

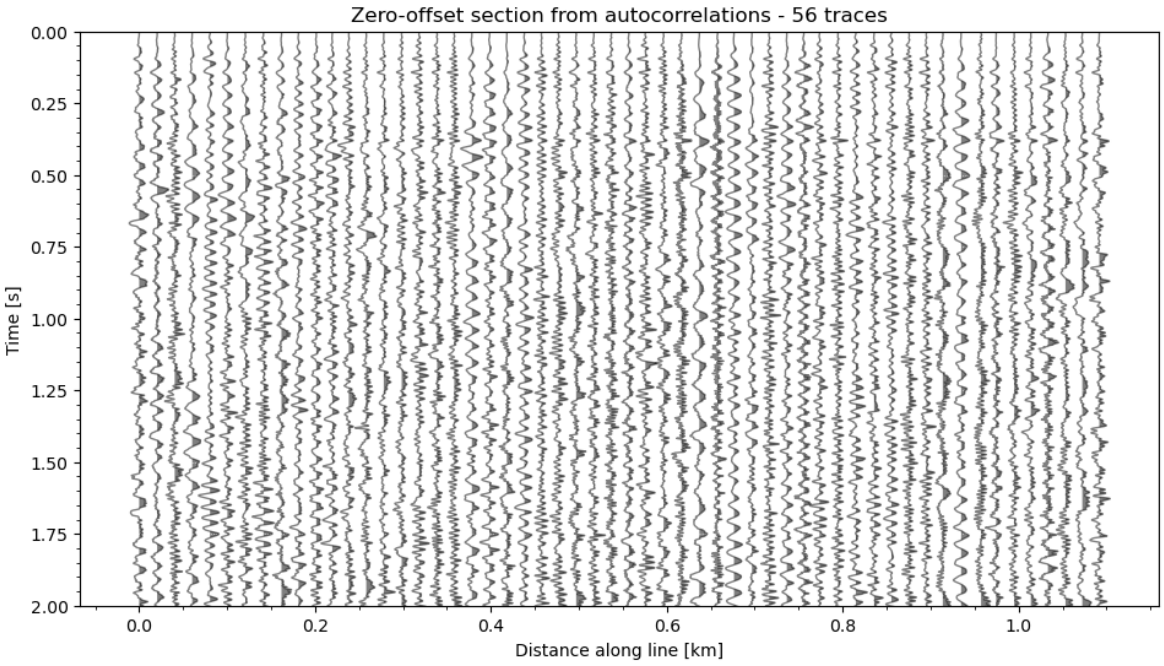

Figure A-1: Section showing the equivalent of image 5-3 for the cross line. The zero-offset section for the cross line resulting from autocorrelations with panels selected with the first illumination analysis.

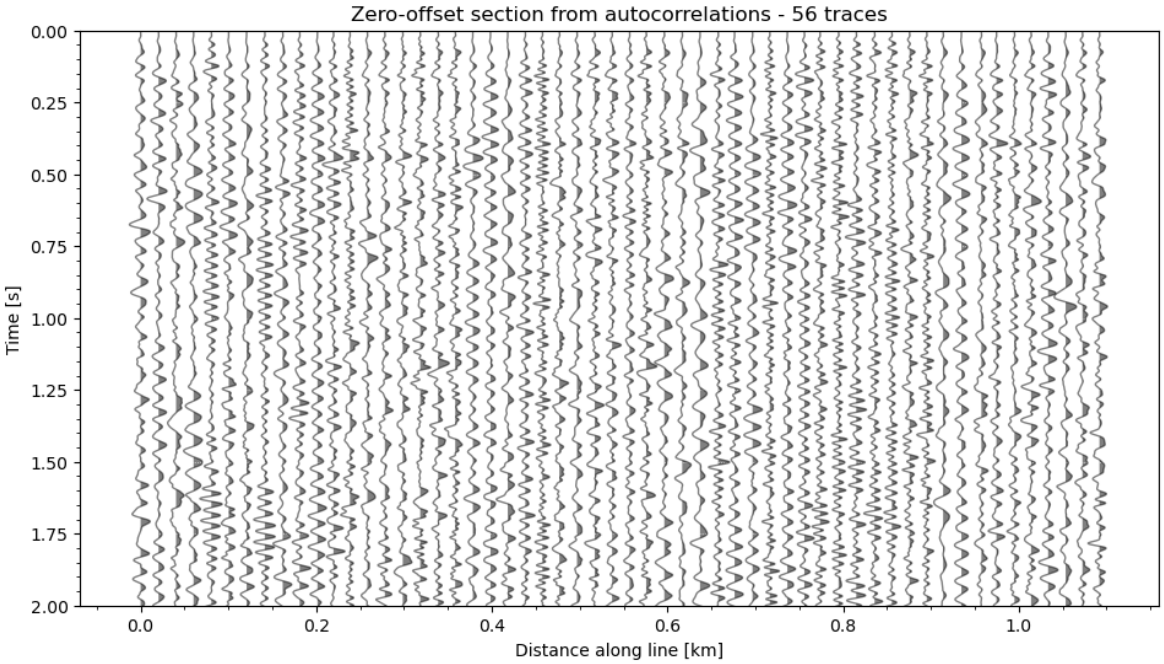

Figure A-2: Section showing the equivalent of image 5-4a for the cross line. The zero-offset section for the cross line resulting from autocorrelations from figure A-1 after filtering with a bandpass filter between 5 and 40 Hz.

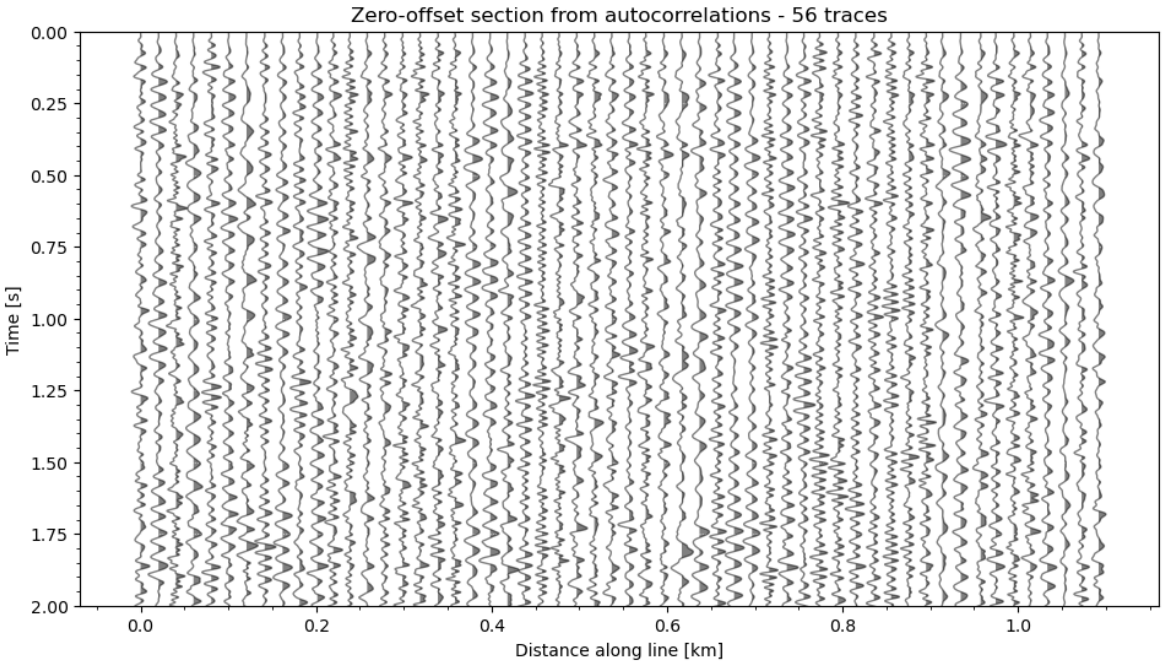

Figure A-3: Section showing the equivalent of image 5-4b for the cross line. The autocorrelated zero-offset section based on illumination analysis with the second filter.

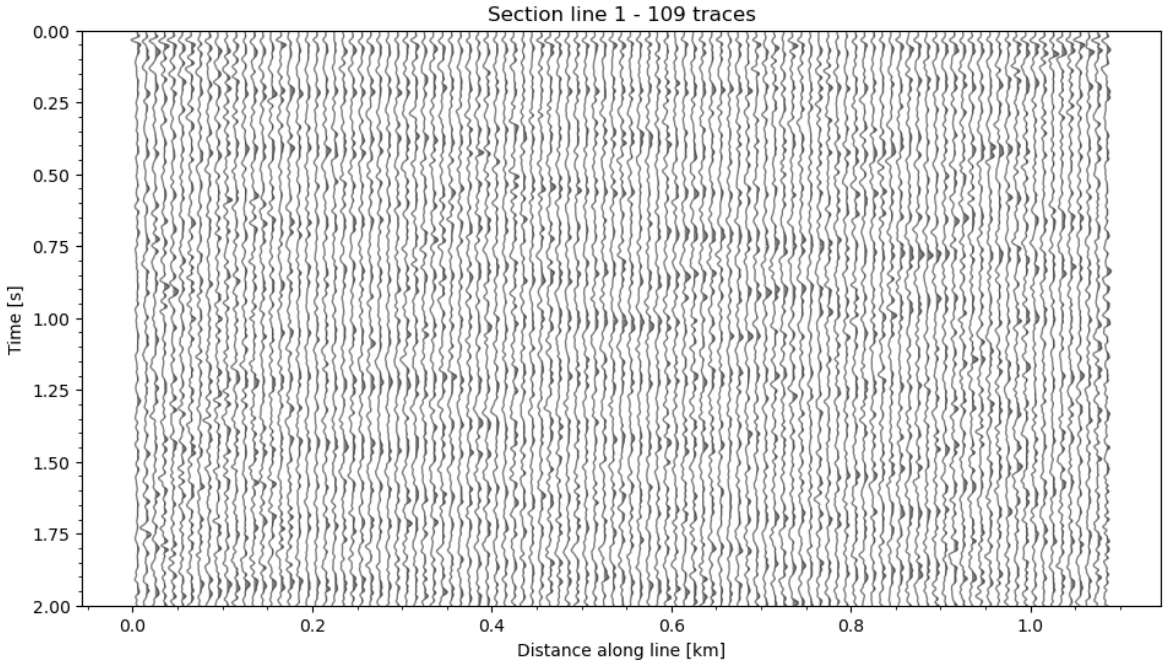

Figure A-4: The stacked section for the cross line that results from stacking the CMP gathers after NMO correction with the velocity picks in table 5-1. Equivalent for the main line can be found as figure 5-8.

A-2 Full sections

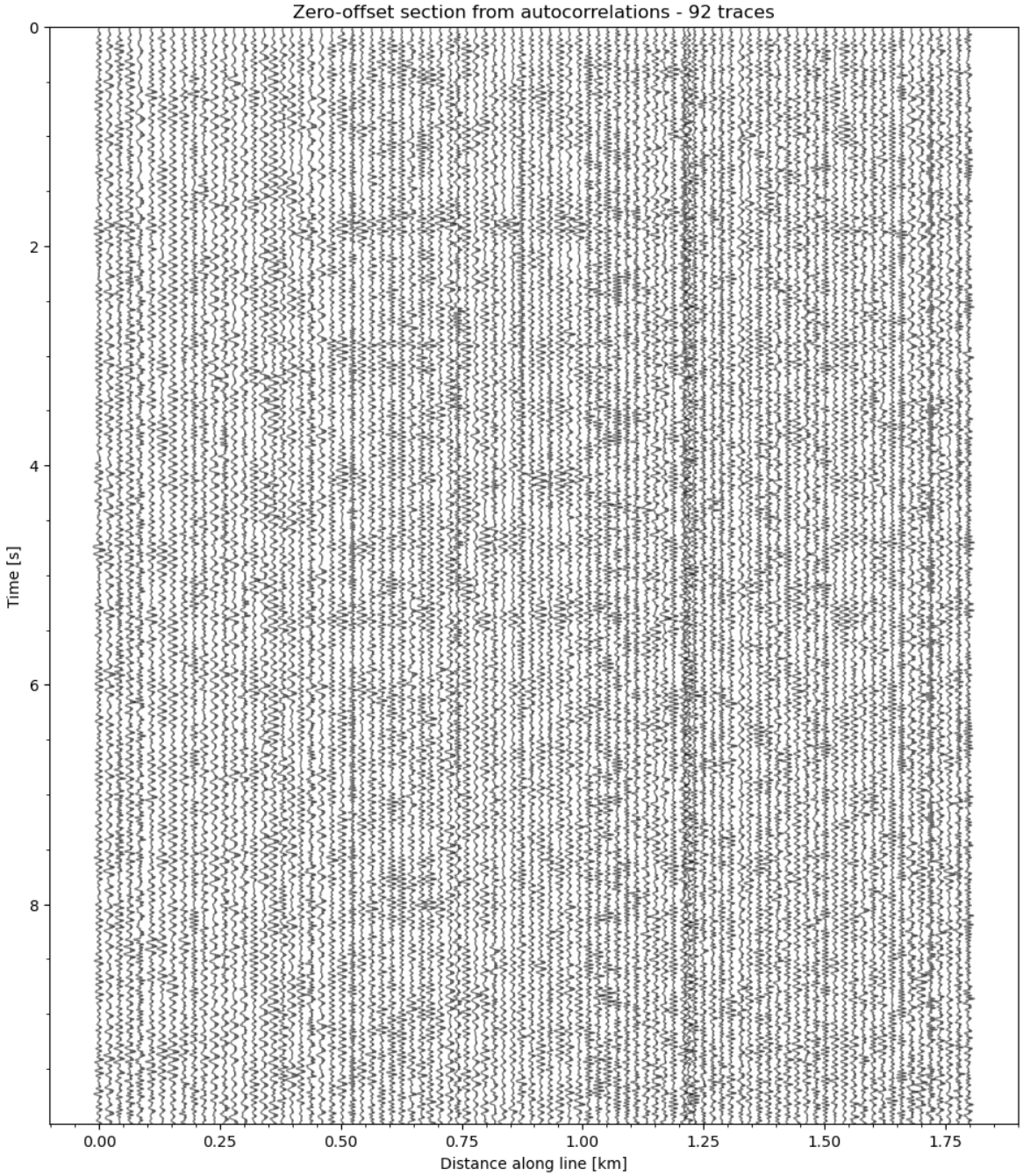

Figure A-5: The full 10-second section for the main line from autocorrelations.

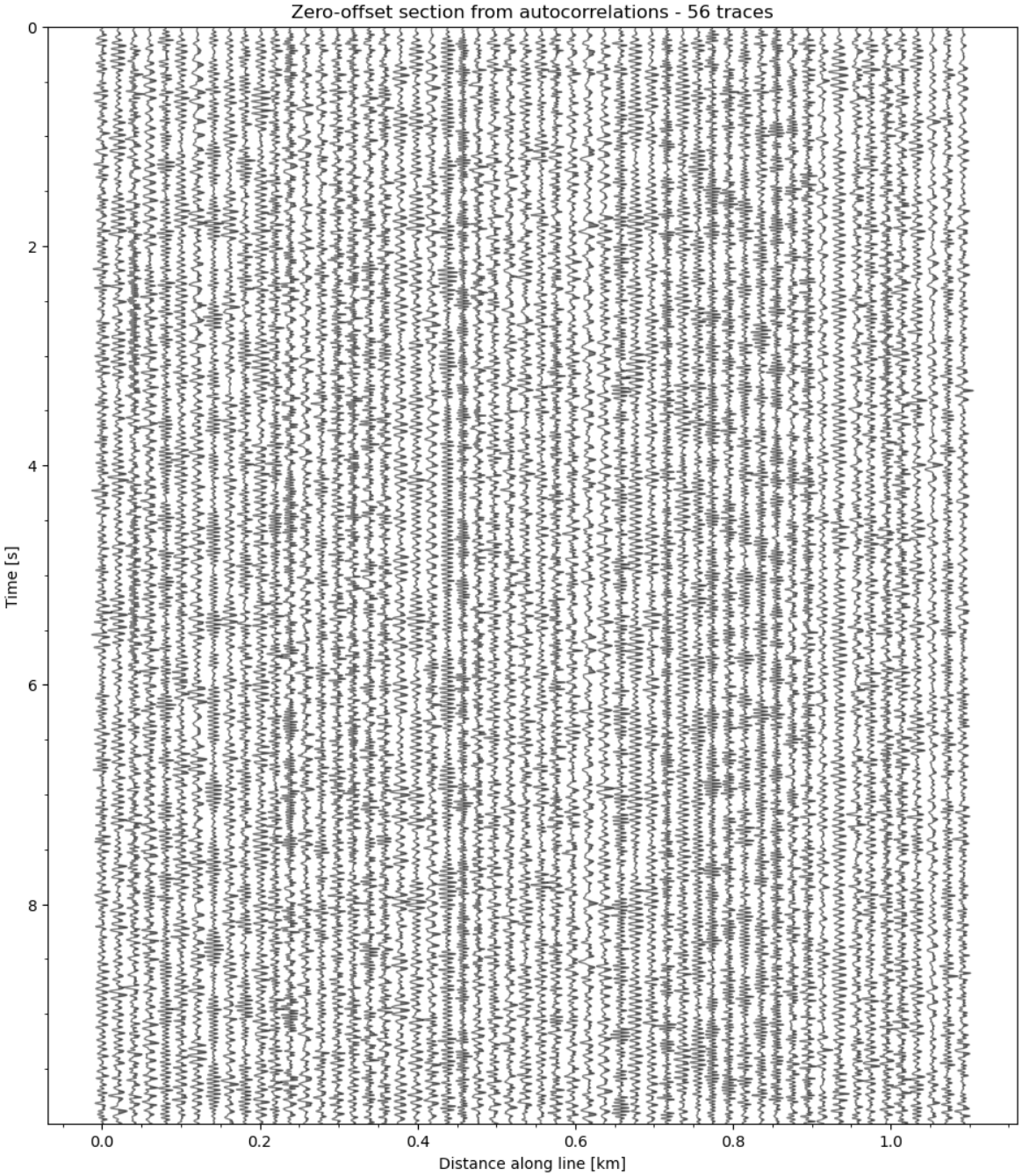

Figure A-6: The full 10-second section for the cross line from autocorrelations.

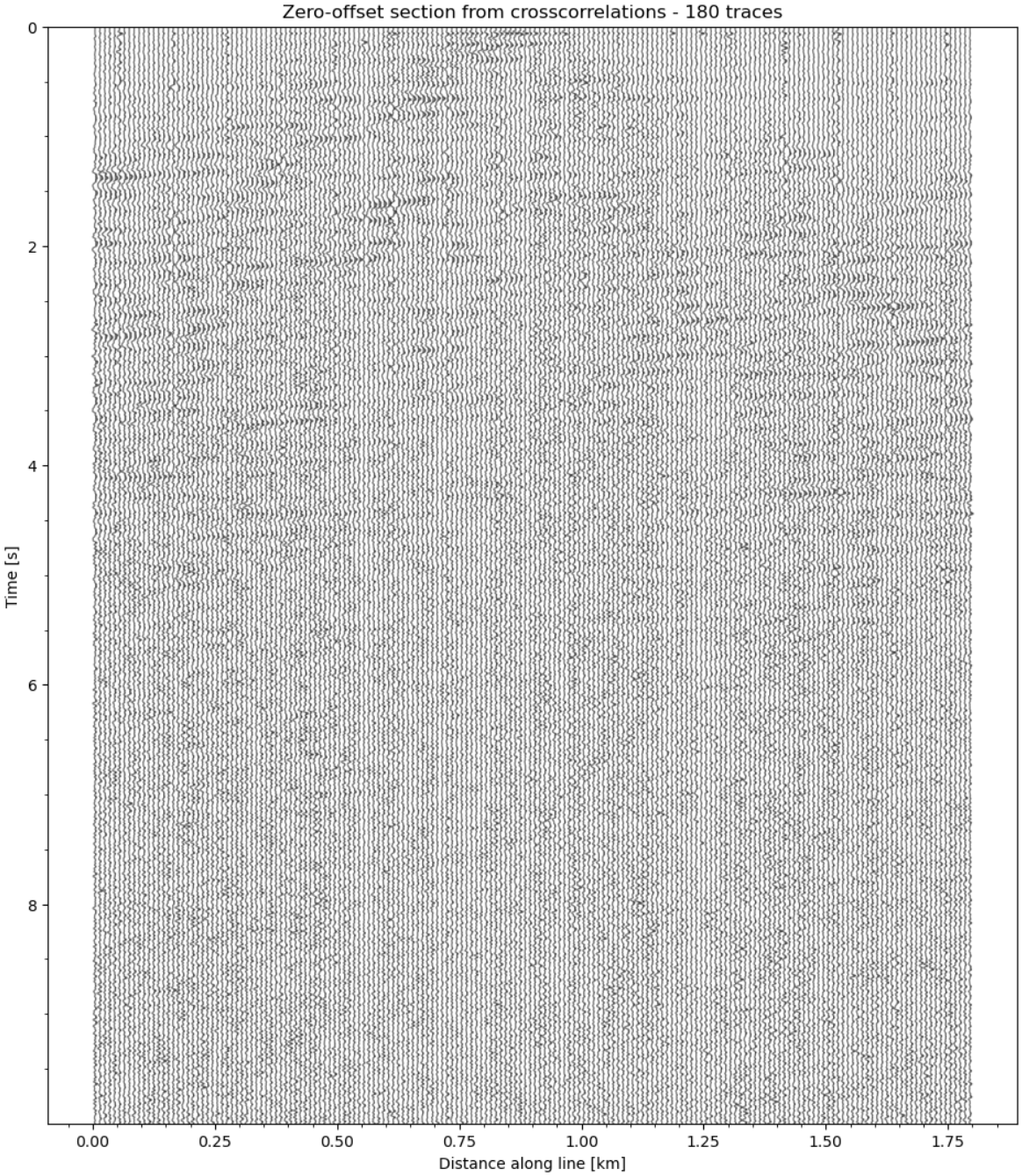

Figure A-7: The full 10-second section for the main line from crosscorrelations.

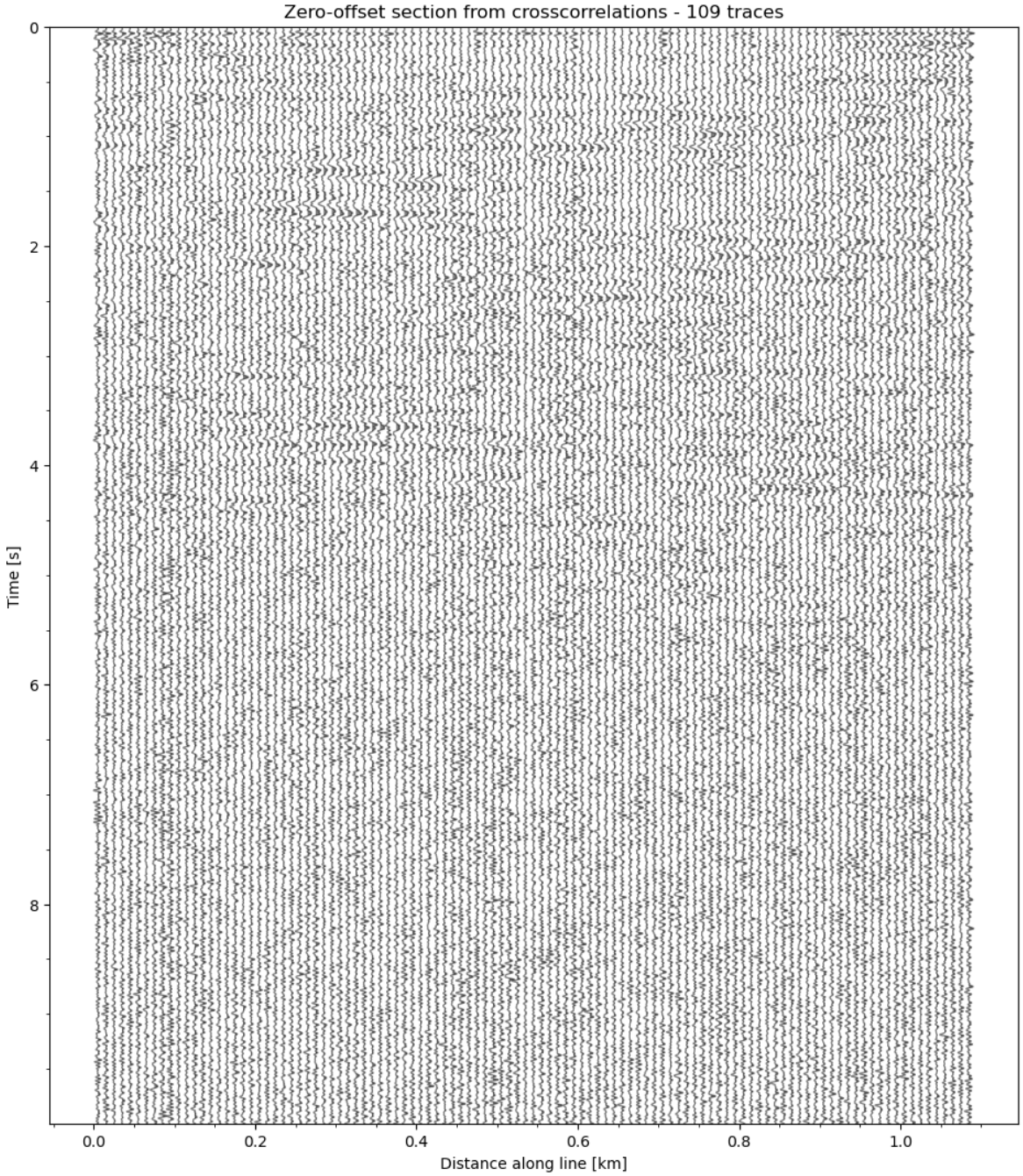

Figure A-8: The full 10-second section for the cross line from crosscorrelations.

Appendix B

Slope correction

The stations were placed on a slight slope. The aim of this appendix is to check whether the slope had a significant effect on the conclusions of the illumination analysis. As a major simplification, the slope is approximated by fitting a line through the elevations of the stations, see figure B-1. The slope angle for lines 0 and 1 is 5.2°and 4.1°, respectively.

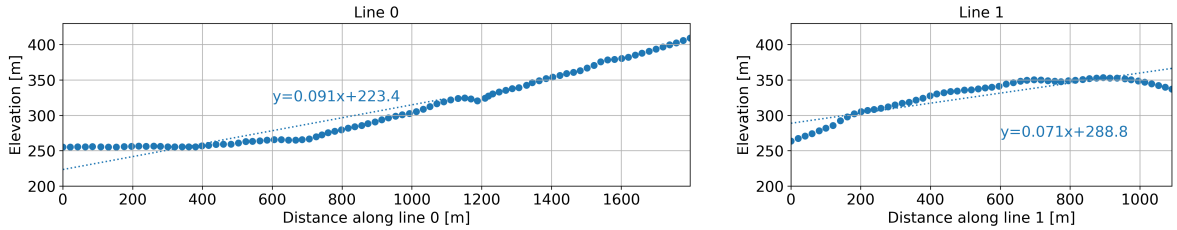

Figure B-1: Elevations of stations (circles) for both lines based on distance from the bottom-most station. A line is fit through this (dotted line) with the equation shown.

The correction for slope is not as easy as it might appear at first. The slowness that is used for the Tau-P transform corresponds to a line in the seismic record (x-t space). The other known quantity is the slope of the hill (x-z space). To convert the slope into a line on the record, the vertical slowness needs to be known.
The problem is that the slowness from the Tau-P evaluation is determined based on the sloped surface, while the vertical slowness should come from a 'true' vertical line. To solve this problem, some other terms must be defined, these are also shown in figure B-2.

The slope of the geophone line is defined as the angle between the ground surface and the local horizontal (α'). Taking the lowest geophone as a reference level, the effect of the elevated geophone line is that at higher geophones, events arrive later. If we assume that the vertical seismic velocity is constant in the near surface, the correction for this would be a linear time shift. This correction is shown as the inclined black line in figure B-2b. The corrected record as recorded on the local horizontal is shown in red in the same figure. The angle between these is called α.
The Tau-P analysis sums up the energy over lines (dashed black line) through the seismic

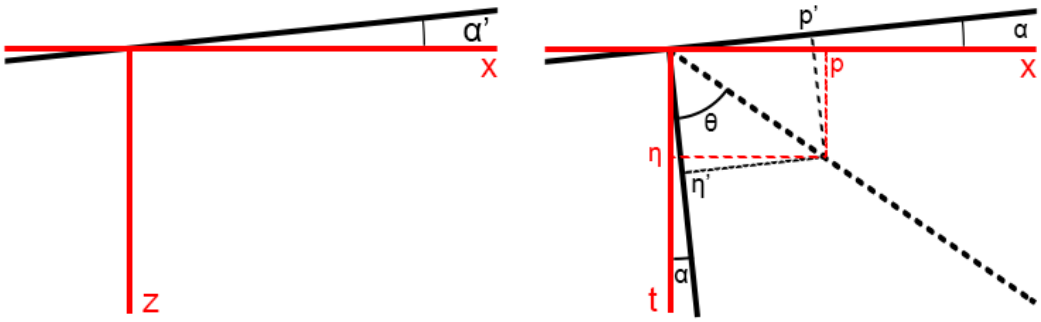

(a) x-z space **(b)** x-t space

Figure B-2: Different terms defined to correct the Tau-P slowness. The red terms x, t and z indicate the axes of each system. α' represents the slope of the geophone line in x-z space, α the slope caused by this in x-t space. p represents the true horizontal slowness and η the true vertical slowness. An apostrophe is added for the apparent slowness. θ is the angle of incidence that is used when not considering the effects of the slope.

record. The angle of incidence of these lines (θ) is based on the wrong vertical line. We can also define a horizontal (p') and vertical (η') slowness associated with the wrong angle of incidence.
The correct angle of incidence would be obtained by adding the angle α to θ when considering events upslope. This would also get the correct horizontal (p) and the correct vertical (η) slowness. These slownesses can be calculated from the angle of incidence i and the seismic velocity v as:

$$\eta = \frac{\cos(i)}{v} \tag{B-1}$$

$$p = \frac{\sin(i)}{v}. \tag{B-2}$$

Calculating α can be done with the assumption that the vertical seismic velocity (and thus vertical slowness η) is constant in the near surface. The time difference due to the elevation after unit distance is $\tan(\alpha')\eta$. Then, the angle is calculated as:

$$\alpha = \arctan\left(\tan\left(\alpha'\right)\eta\right). \tag{B-3}$$

The apparent angle of incidence θ can simply be calculated with p' and equation B-1:

$$\theta = \arcsin\left(p'v\right). \tag{B-4}$$

We use the true angle of incidence $(\alpha + \theta)$ in the definition η from eq. B-1:

$$\begin{aligned}\eta &= \frac{\cos(\alpha+\theta)}{v} \\ &= \frac{1}{v}\left(\cos(\alpha)\cos(\theta) - \sin(\alpha)\sin(\theta)\right)\end{aligned} \tag{B-5}$$

Before putting in the definitions of both α and θ, we look at the definitions of the cosine and

sine of inverse goniometric functions:

$$\begin{aligned} \cos(\arctan(x)) &= \frac{1}{\sqrt{x^2+1}} & \cos(\arcsin(x)) &= \sqrt{(1-x^2)} \\ \sin(\arctan(x)) &= \frac{x}{\sqrt{x^2+1}} & \sin(\arcsin(x)) &= x \end{aligned} \tag{B-6}$$

$$\downarrow$$

$$\begin{aligned} \cos(\alpha) &= \frac{1}{(\tan(\alpha')\eta)^2+1} & \cos(\theta) &= \sqrt{1-(p'v)^2} \\ \sin(\alpha) &= \frac{\tan(\alpha')\eta}{(\tan(\alpha')\eta)^2+1} & \sin(\theta) &= p'v \end{aligned} \tag{B-7}$$

All of this information is combined by putting eq. B-7 into eq. B-5:

$$v\eta = \underbrace{\frac{\sqrt{1-(p'v)^2}}{\sqrt{(\tan(\alpha')\eta)^2+1}}}_{\cos(\alpha)\cos(\theta)} - \underbrace{p'v\frac{\tan(\alpha')\eta}{\sqrt{(\tan(\alpha')\eta)^2+1}}}_{\sin(\alpha)\sin(\theta)} \tag{B-8}$$

$$\eta = \frac{\frac{1}{v}\sqrt{1-(p'v)^2} - p'\tan(\alpha')\eta}{\sqrt{(\tan(\alpha')\eta)^2+1}} \tag{B-9}$$

$$\eta\sqrt{(\tan(\alpha')\eta)^2+1} = \frac{1}{v}\sqrt{1-(p'v)^2} - p'\tan(\alpha')\eta \tag{B-10}$$

$$\eta^2\left((\tan(\alpha')\eta)^2+1\right) = \frac{1}{v^2}\left(1-p'^2v^2\right) - 2\frac{1}{v}\sqrt{1-(p'v)^2}p'\tan(\alpha')\eta + p'^2\tan^2(\alpha')\eta^2 \tag{B-11}$$

$$\begin{aligned} \eta^4\tan^2(\alpha') + \eta^2 = \eta^2p'^2\tan^2(\alpha') &+ \eta\left(-2\sqrt{1-(p'v)^2}\frac{p'}{v}\tan(\alpha')\right) \\ &+ \left(\frac{1}{v^2} - (p')^2\right) \end{aligned} \tag{B-12}$$

$$\begin{aligned} 0 = \eta^4\left(\tan^2(\alpha')\right) + \eta^2\left(1-p'^2\tan^2(\alpha')\right) \\ + \eta\left(2\sqrt{1-(p'v)^2}\frac{p'}{v}\tan(\alpha')\right) + \left(p'^2 - \frac{1}{v^2}\right) \end{aligned} \tag{B-13}$$

Equation B-13 is a fourth-degree polynomial that can be solved for η. For clarity, the terms are:

$$\begin{aligned} a &= \tan^2(\alpha') \\ b &= 0 \\ c &= 1 - p'^2\tan^2(\alpha') \\ d &= 2\sqrt{1-(p'v)^2}\frac{p'}{v}\tan(\alpha') \\ e &= p'^2 - \frac{1}{v^2} \end{aligned} \tag{B-14}$$

With the true vertical slowness, the true horizontal slowness can be determined. This is the end result:

$$p = \frac{1}{v^2} - \eta^2. \tag{B-15}$$

It was shortly mentioned that the new angle of incidence was used for the line upslope. Similar calculations can be done for the line downslope. This would give a new angle of incidence of $(\theta - \alpha)$. The calculations themselves are left out, as they are very similar to the previous ones. The result shows that only the factor d in eq. B-14 is changed by adding a minus.
Because the directions have different correction factors, this cannot be applied after calculations are done. We will first look at how large the errors are, before deciding whether or not to apply the correction.
Two quantities need to be known to apply the results. The slope is known - it is 5.1°. The seismic P-wave velocity near the surface is the same as the velocity used for the calculation of panel length (1800 m/s). With this, the results show that a larger surface slope, means a larger difference between the true and apparent slowness values. The results for the larger slope can be seen in figure B-3.

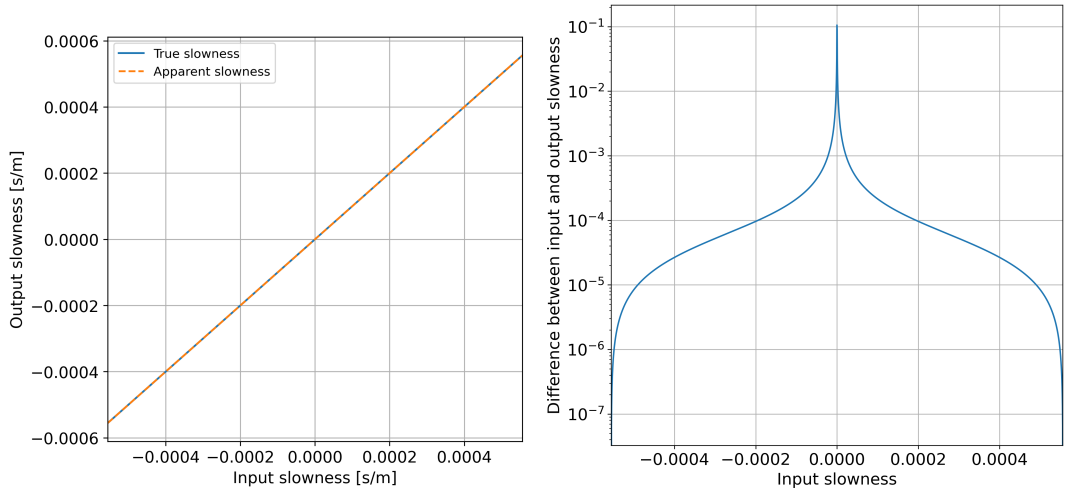

Figure B-3: The equation for the true horizontal slowness applied with a slope of 5.1° and a near-surface velocity of 1800 m/s.
(a) Both true and apparent slowness plotted against the apparent slowness.
(b) Relative error of the apparent slowness compared to the true slowness. A logarithmic axis is used for the y-axis.

The results show that the two slowness values are very close together. Only near the point of zero slowness does the relative error rise to around 10%. The average error over the range of slowness values sampled is 0.043%. As this error is smaller than the step in slowness values that are sampled, the error due to elevation is not considered.

Appendix C

Research module

August 5, 2022

Overview of the applicability of different seismic interferometry sources to monitor CO_2 after reinjection

Sverre Hassing

Supervisors:
Deyan Draganov (D.S.Draganov@tudelft.nl)
Martijn Janssen (M.T.G.Janssen@tudelft.nl)

January 2022

1 Abstract

In the context of global climate change, the reduction of CO_2 emissions from energy production is an important topic. Emissions caused during geothermal energy production can be reinjected into the original reservoir to reduce the amount released into the air. This is done at the Hellisheidi site in south-western Iceland. The CO_2 must be monitored after it has been injected. Passive seismic interferometry (SI) is a promising method for this, as no source campaigns are necessary. To prepare for an upcoming investigation, where actual data from the site will be processed, different methods of SI are discussed and their applicability evaluated.
Surface wave SI only provides tomographical images. These also have a lower resolution than active reflection images. Global earthquake SI (with global-phase or teleseismic arrivals) gives a low resolution, due to the low frequency content of arrivals, and needs a long recording time to get a good illumination range. Body wave ambient noise SI requires extra methods to isolate body wave energy from the dominant surface wave energy, but provides a promising method. Due to an abundance of local seismicity in Iceland, local earthquake SI is deemed the best fit for the monitoring process.

2 Introduction

Geothermal energy, utilising heat from inside the Earth for power generation and heating, can play an important role in the transition to more sustainable energy sources. It is associated with less greenhouse gas emissions than energy generation with fossil fuels, however, there are still some emissions, particularly of CO_2 (Sass and Duffield, 2003). To reduce these, the greenhouse gases can be captured, so that they are not released into the air. This requires some storage medium. reinjection of the CO_2 into an underground reservoir, also called carbon capture and sequestration (CCS), is a prominent method for this (Haklidir et al., 2019).
The reinjection can be done in two ways. The first is in a buoyant phase, either in gaseous form or as a supercritical fluid. This way, the CO_2 will float on top of the formation fluids, so an important consideration is that the reservoir must have a good seal, to prevent leakage back to the surface. Afterwards several different trapping mechanisms bind the CO_2 underground (see fig. 1), where the most long-term one is precipitation as minerals, which can take from decades to centuries (Benson and Cole, 2008).

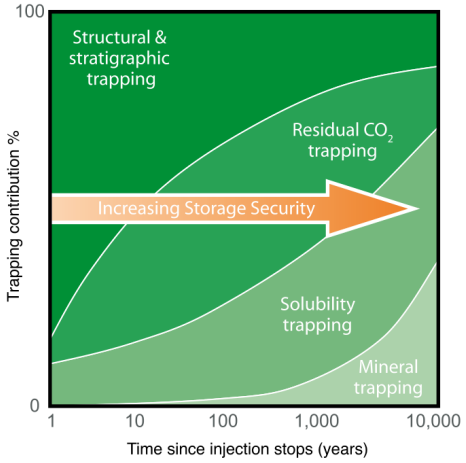

Figure 1: Different trapping mechanisms for CO_2 throughout time with their relative contributions as a general overview. Figure gotten from Metz et al., 2005, p. 208.

The other reinjection method is used by dissolving the CO_2 into water before or during the injection. This method was investigated with trial runs in the CarbFix projects (Matter et al., 2015, Sigfusson et al., 2015) at the Hellisheidi geothermal site in southwestern Iceland near Reykjavik (see fig. 2). This method should not have the same leakage problems as the buoyant version, as the CO_2 is already dissolved. It also means that mineral precipitation should happen faster, because the process starts off with solubility trapping.
Another added benefit is that without reinjection, the reservoir pressure would drop as CO_2 is being removed from the system, lowering the productivity (Stork et al., 2020). Reinjection keeps up the pressure.
As a follow-up to the first CarbFix project, the Synergetic Utilisation of CO_2 storage Coupled with geothermal EnErgy Deployment (SUCCEED) project is set up to monitor both injection techniques at the geothermal sites at Hellisheidi and at Kızıldere in Turkey (Durucan et al., 2021).

Figure 2: Location of the Hellisheidi geothermal site indicated on a map of Iceland. From OpenStreetMap.

One of the possible monitoring methods at the Hellisheidi site is seismic interferometry. Although the method can also be used with active sources, passive methods give some distinct advantages (Wapenaar et al., 2010). As implied by the name, no active source campaign is necessary, instead various different signals that would normally be considered noise and happen by themselves can be utilised. This makes the method a lot cheaper and better suited for monitoring.
This research is conducted as an initial investigation into the sufficiency of various methods of passive seismic interferometry for monitoring the CO_2 injection at the Hellisheidi site. During the summer of 2021 a week of passive data was recorded at the site. The recording also contains the results of an active survey, a local earthquake of M_W 5.0 and one of M_W 8.2 in Alaska.
A literature study is done to collect the various advantages and disadvantages of different passive SI methods with different sources, such as surface waves, body wave ambient noise, global and local earthquakes. All of these methods will be considered separately at first. Then the different characteristics are collected and they are judged based on the specific characteristics of the data and the site. In the main investigation (as part of a Master's thesis), the appropriate methods are applied to the recorded data to show the usefulness for monitoring injected CO_2.

3 Methods

Seismic interferometry (SI) is a method to obtain virtual source records between two receiver stations by crosscorrelating the record from one station with that of the other. The method is originally based on Claerbout, 1968, where the principle for a one-dimensional case was developed. Later it was further developed for three-dimensional cases (Wapenaar et al., 2004).
When a source outside of the two stations emits a signal, it is recorded at the first station, travels further and is recorded at a second station, see figure 3. Crosscorrelating the records of the two stations gives a new record that effectively removes the shared path of the signal. This results in something that can be interpreted as the record of the second station if there had been a source at the first station (Wapenaar et al., 2010).
This can be done for both surface and body waves (as also seen in fig. 3). For body waves, which reflect off the surface, this gives zero-offset reflection images, which can be further processed with normal seismic processing workflows. For surface waves, this method can solve some problems with source distributions and location determination (Yang et al., 2007). Surface wave tomography, however, gives a different kind of image of the subsurface, there will still be a short bit about the method for completeness.

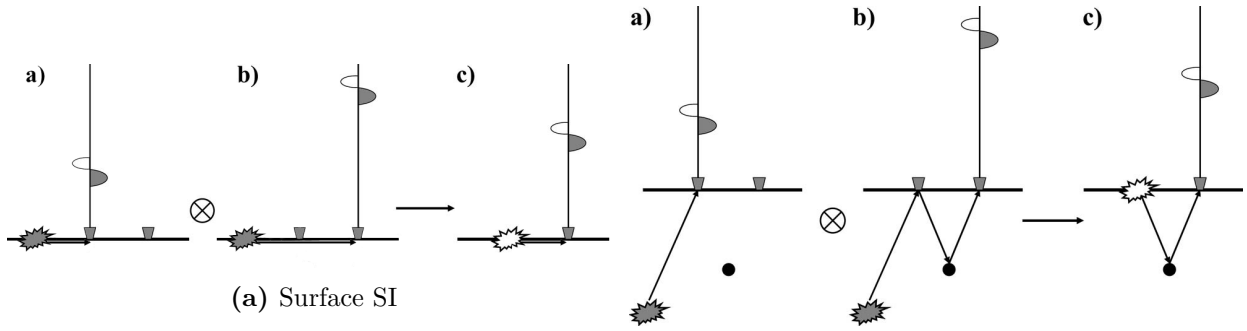

(a) Surface SI

(b) Reflection SI

Figure 3: Figure 3b is from Wapenaar et al., 2010, originally from Schuster, 2009, figure 3a is adapted from this. It shows the same concept explained for waves travelling along a surface and for reflection SI. Above the stations, the recorded trace can be seen.
For both cases, a) shows a signal from the source reaching the first station, b) shows the same signal travelling further and reaching the second station, between them is a $\otimes$ indicating a crosscorrelation, which results in c) the resulting trace at the second station can be seen as if caused by a virtual source at the location of the first station.

The relation underlying SI can be defined as (Draganov and Ruigrok, 2014, originally from Wapenaar and Fokkema, 2006):

$$G^{v,f}_{p,q}(\mathbf{x}_B, \mathbf{x}_A, t) + G^{v,f}_{p,q}(\mathbf{x}_B, \mathbf{x}_A, -t) \approx \frac{2}{\rho c^K} \int_{\partial D_1} G^{p,K}_{v,\phi}(\mathbf{x}_B, \mathbf{x}, t) * G^{q,K}_{v,\phi}(\mathbf{x}_B, \mathbf{x}_A, -t) d^2\mathbf{x} \tag{1}$$

G indicates the Green's function between two stations as indicated by their locations $G(\mathbf{x}_{rec}, \mathbf{x}_{src}, t)$. The super and subscripts describe the source (f) direction (q) and the receiver direction (p) measured as a particle velocity (v). ∂D_1 is a surface of P- or S-wave sources (ϕ) with density (ρ) and seismic velocity (c^K) that surrounds the stations. The K can take values from 0 to 3 and indicates a P-wave or three directions of movement for S-waves. The $*$ indicates a convolution, with the $-t$ making it a crosscorrelation.
The interpretation of the equation is that there is a boundary surrounding the receivers with P- and S-wave sources at different locations. The waves emitted from these are recorded at receivers A and B. The records from both are crosscorrelated and the results from the different sources are added together. This would be equal to the record recorded at receiver B with a source at receiver A. It contains a causal and an acausal part. Added together the full Green's function is obtained.
There are a couple of assumptions made for this equation regarding the boundary (Wapenaar and Fokkema, 2006, Draganov and Ruigrok, 2014):

- The sources on the boundary are in the far field of the receivers.
- The density and velocity outside of the boundary change smoothly.
- The density and velocity on the boundary are constant.

Most of these can be satisfied if the boundary is very far away and the receivers are located on a free surface. In reality, most of the sources will not be equally distributed on some boundary, but focused on some locations. This will still work if the scatterer density is constant and the waves travel isotropically near the receivers (Snieder, 2004).

3.1 Surface waves

Seismic interferometry with ambient noise to find surface waves is one of the methods that developed and rose to prominence a bit earlier than other methods, see Shapiro and Campillo, 2004 or Shapiro et al., 2005. In most frequency bands, the noise is dominated by surface waves (Draganov et al., 2013). This makes processing of this data a lot easier, as the signal does not have to be uncovered from other noise. To improve the imaging, it is still worthwhile to remove other signals, so the body waves, from the records (Bensen

et al., 2007). Another signal that is generally filtered out, is noise from microseisms (caused by motion in the oceans in two frequency bands), although this in itself can also be used for the interferometry (Sabra et al., 2005, Ruigrok et al., 2011).
Imaging with surface waves is fundamentally different from reflection imaging. Surface waves are dispersive, so different frequencies travel at different velocities. Lower frequencies are also more sensitive to greater depths (Stein and Wysession, 2003). This leads to different group and phase velocities for waves with different periods. The difference in phase and group velocity with depth is related to P- and S-wave velocities.
Based on this information, tomography can be done to get deeper information on regional to global scales (Yang et al., 2007). Another important thing to note is that the values obtained are averages over larger areas (Shapiro and Campillo, 2004), so resolution on reservoir scale is relatively low.

3.2 Body wave ambient noise

Ambient noise is a vague descriptor of signals from various different sources, both natural and artificial, that in a normal reflection survey would obscure the desired signal. This could be from various human activities, such as from roads or construction work, but also from local seismicity or random noise with no clear origin known, as long as there is a good illumination from all directions.
The processing for random noise is slightly different than for distinct events. As long as the sources are uncorrelated, no crosscorrelation and subsequent summation of all sources is needed (Wapenaar and Fokkema, 2006). Instead, the noise can be crosscorrelated once (Wapenaar et al., 2010).
To get reflection images, body waves are needed, but as mentioned, in most frequency bands, the noise is dominated by surface waves. In Draganov et al., 2009, a bandpass filter and an f-k filter are used to suppress the surface waves, but afterwards all of the noise is summed up to get the final image.
Draganov et al., 2013 expand on this by processing only the panels in which body waves are recognised. This increased the signal-to-noise ratio, but limited the illumination. Both the methods of crosscorrelating all of the noise (Boullenger et al., 2015, Cheraghi et al., 2015) and selecting the panels dominated by body waves (Panea et al., 2014, Nakata et al., 2015) can be found in later literature. A couple of different methods to isolate the body-wave energy will be discussed.
To go back to Draganov et al., 2013, the body wave detection was done with beamforming analysis. This gives the slowness spectrum over azimuth. The dominant slowness and the direction gives an indication if the event is likely to be caused by a body wave based on the direction at arrival.
Various different variations on the beamforming process are available. For example, multirate beamforming (Corciuolo et al., 2012), double beamforming (Nakata et al., 2016) or radial distance beamforming (Roots et al., 2017).
Two different basic machine learning methods (k-means clustering (Chamarczuk et al., 2020) and support vector machines (SVM, Chamarczuk et al., 2019)) can also be found, where based on already filtered data, body wave events in the noise are detected automatically. K-means clustering finds a specified (k) amount of different clusters of data by seeing which data point is the closest to each centre. Then the centres are updated and repeat until some convergence. This gives different noise clusters that are associated with different interpretations. An SVM tries to find the hyperplane separating two clusters. This is used afterwards as a decision boundary for two options (in this case either body wave or not). The data can be mapped to some non-linear domain, where the data is linearly separable, for extra flexibility.

3.3 Global earthquakes

Earthquakes are recorded as distinct events that stand out from the noise. The original relation for SI can be used for them, meaning that the crosscorrelations from each event are added together to improve the quality of imaging. Earthquake arrivals are complicated and drawn out, as the wavefronts split up travelling through Earth. This gives different phases that arrive at different times. These arrivals can be used separately for SI. Their name is collected based on based on their interactions with the various boundaries of the inner Earth (see fig. 4).
For SI, a distinction is made between waves that have travelled through the core (e.g. PKP, PKIKP), which are called global-phase, and those that have only travelled through the mantle (e.g. P, PcP), called teleseismic waves.

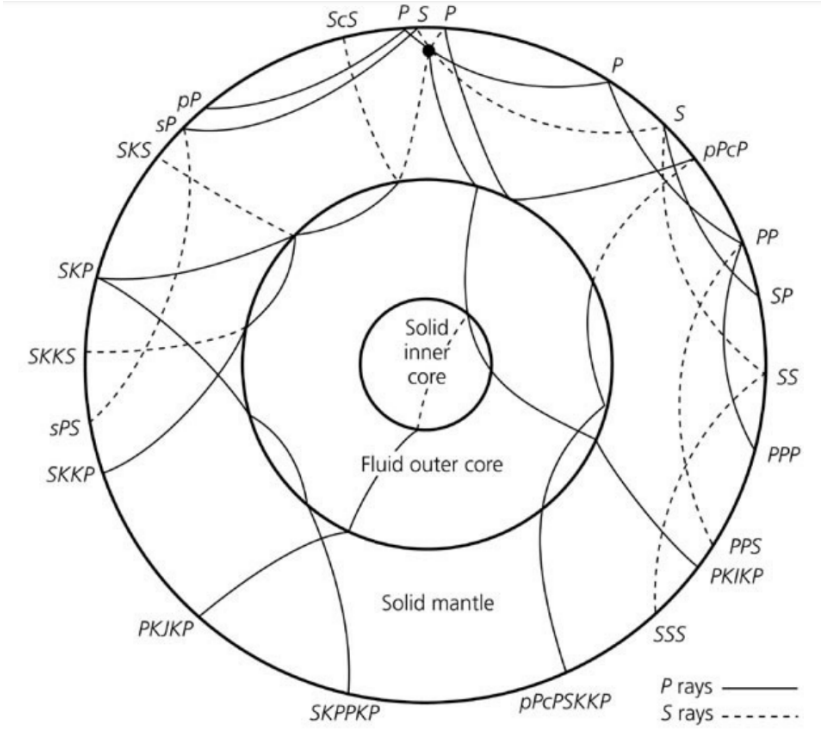

Figure 4: Different global phases after reflection and refraction off different boundaries in the Earth. The source can be seen as the black dot in the top of the picture. The name of a phase is built up as a combination of all of the different interactions that the ray path goes through before reaching the surface.
A capital P or S indicates a direct ray path, a lower case p or s that the ray path went upwards from the source and reflected off the surface first. K and I are P waves travelling through the outer and inner core respectively, J is an S wave travelling through the inner core. c means a reflection off the outer core and i a reflection off the outer core.
Picture gotten from Stein and Wysession, 2003, p. 165.

A method adapting global-phase arrivals for seismic interferometry called GloPSI was developed in Ruigrok and Wapenaar, 2012. It was subsequently used for various investigations into crust and upper mantle properties around the world (Nishitsuji, Ruigrok, et al., 2016, Andrés et al., 2019, Bianchi et al., 2021).
The method assumes that the incoming waves are almost planar and travel vertically with the lithosphere being layered horizontally. Of course, this is not the case realistically, so extra events show up on the image. These are suppressed by summing the responses from a range of sources, the illumination range. Ruigrok and Wapenaar, 2012 mention that ray parameters between 0 and 0.04 s/km are enough. Earthquakes with a magnitude above 6 (in the original relaxed to $M > 5.5$) are selected.
Another problem is that, especially longer after an earthquake, the different phases start arriving at the same time, causing problems for the crosscorrelation. Time windows are selected that are dominated by one ray parameter to prevent this.
After the selection, the phase responses at a station are all autocorrelated and added together. Afterwards, some extra processing is done, such as removing coherent events across the stations, which is possible if the terrain is heterogeneous enough, so that no signal is removed.
Due to the long ray paths, low frequencies dominate for global phases, giving a low resolution (Ruigrok and Wapenaar, 2012).

There is no such single algorithm that has been developed for teleseismic waves, although the processing is similar. For example, in Nishitsuji, Rowe, et al., 2016, the method is based on GloPSI, but the coda of teleseismic P-waves are used. Here, seismic interferometry was applied to deep moonquakes. Although the epicentral distances are quite short, varying between 3.2 and 14.7°, they still conform to the strict

definition of teleseismic waves, travelling through (and originating in) the mantle and not the core. These close moonquake clusters are selected so that the waves arrive nearly vertically at the stations.
Similarly, in J. A. Casas et al., 2020, teleseismic waves are used that arrive nearly vertically. A required ray parameter of less than 0.08 s/km gives epicentral distances between 30 and 120°. For a good signal-to-noise ratio, magnitudes greater than 6.0 are selected. Abe et al., 2007 do not mention their criteria for the teleseismic waves, except for magnitudes between 6.2 and 7.0. Their synthetic example uses ray parameters from 0.048 to 0.074 s/km. Lastly, in Tonegawa et al., 2009 coda from S waves are used from epicentral distances between 30 and 85° with magnitudes between 5.5 and 7.5.

3.4 Local earthquakes

Local earthquakes cover a large range of seismicity. The global earthquakes were required to have a certain minimum magnitude to still be able to distinguish them. The local earthquakes travel a shorter distance to the receivers, so the signal is less attenuated. Microseismicity can provide enough information to make an image, but be difficult to distinguish from the other noise. It is also an important source for the ambient noise as mentioned previously. The distinction between local earthquake SI and body wave ambient noise SI is that former looks for specific events for the crosscorrelation, while the latter accepts all noise, with a possible filter for body waves.
Compared to global earthquake SI, the possibility to use smaller events, both expands and limits the options. In seismically active areas, there are a lot more small events, so recordings can be shorter and the resolution higher. On the other hand, in seismically inactive areas, there are fewer events and signals from further away are unlikely to have a high enough signal-to-noise ratio. The local events also allow the method to use higher frequency data, giving a better resolution for more shallow structures (Nishitsuji, Minato, et al., 2016).
These requirements also show up in the applications. Most literature dealing with interferometry from local earthquakes is applied in volcanically active areas, often to determine the structure of the volcano and its magma chambers.
In older literature (Daneshvar et al., 1995, Scherbaum, 1987), interferometry with micro- or local earthquakes was done in areas with simple geometries to conform to the original formulation for 1D media. This required horizontal layering and events with a nearly vertical incidence.
More modern methods also aim to work with more heterogeneous terrain. One of the problems encountered is that the distribution of the earthquakes is not uniform, but centered on some locations. In Kim et al., 2017, this is resolved by binning the virtual midpoints, otherwise the traces did not show clear and coherent reflectors. During the research, about a thousand earthquakes with magnitudes less than 2.0 were recorded over a month.
Similarly, in J. Casas et al., 2019, a selection of source locations is done to ensure that the waves arrive vertically. This required special relocation software to obtain the rough source locations. A more heterogeneous terrain (more scatterers) requires a less precise location. The data was collected over a year of passive recording. In Polychronopoulou et al., 2020, the source location is estimated based on automatically detected P- and S-wave arrival times. A similar amount of microearthquakes is selected, all lying within 5 km of the virtual source station. Duration magnitudes vary between -1.5 and 2.0.
Nishitsuji, Minato, et al., 2016 use P-wave coda from local earthquakes. They define local as the epicentral distance between 2 and 6°, allowing the P-wave coda to be separated from surface and S-wave energy. A comparison with global-phase images from the same area showed that the resolution is higher for shallow structures, probably due to the higher frequency band that could be used, but that the crust-mantle discontinuity (the Moho) is less clear.

4 Results

Various different characteristics of the various methods are collected in table 1. These are based on a small selection of research for each method. The amount of research is not comprehensive, so the table gives a first indication of the requirements for the different methods.

Source type							References
Surface waves	Recording time [months]			Minimum signal-to-noise ratio	Max. period [s]		
	4 - 12			4 - 10	25 - 150		Yang et al., 2007, Shapiro and Campillo, 2004, Shapiro and Campillo, 2004, Benson and Cole, 2008
Ambient noise	Recording time		Panel length [s]		Imaging depth [km]	Number of panels	
	11h - 10d		16s - 2h		0.5 - 1.2	300 - 1200	Draganov et al., 2013, Nakata et al., 2011, Nakata et al., 2015, Panea et al., 2014, Cheraghi et al., 2015
Earthquakes	Recording time [months]	Epicentral distance	Magnitude	Incidence angle	Imaging depth [km]	Number of events	
Global-phase	7 - 12 (48 for Hi-Climb)	$> 120°$	$M > 5.0$ - 5.6	<0.04 - 0.06 s/km	100 - 300	34 - 81	Andrés et al., 2019, Bianchi et al., 2021, Nishitsuji, Ruigrok, et al., 2016, Ruigrok and Wapenaar, 2012
Teleseismic	3 - 12	25 - 30 to 85 - 120°	$M > 5.5$ - 6.0 ($M < 3.0$ for Moon)	$<$ 0.012 - 0.08 s/km	60 - 160	24 - 59	J. A. Casas et al., 2020, Abe et al., 2007, Nishitsuji, Rowe, et al., 2016
Local	2 - 12	$<$ 6' $\vee$ 2 - 6°	$-1.5 < M < 2.0$ $\vee$ $3.3 < M < 6.5$	$<$ 3 - 20°	3 - 8	42 - 989	Daneshvar et al., 1995, J. Casas et al., 2019, Kim et al., 2017, Nishitsuji, Minato, et al., 2016, Polychronopoulou et al., 2020

Table 1: A summary of the different conditions used for data used as input in seismic interferometry using different sources based on the literature.

5 Discussion

The first consideration is whether or not to use surface wave SI. The imaging method is entirely different compared to the reflection imaging of the body wave methods. Surface wave imaging gives averaged images over regional areas, especially due to the tomographical approach. This gives information on the local geology, but not on specific characteristics of a reservoir, which is needed for the CO_2 monitoring.
A comparison in the available literature shows that most of the monitoring done previously was with reflection imaging (Eiken et al., 2000, Whittaker et al., 2011, Furre et al., 2017) rather than surface wave tomography (Ikeda et al., 2016, Ikeda et al., 2018). Add to this, that active source reflection data was gathered along the same line. Thus, because it is expected to deliver worse results and because it cannot easily be compared to the already existing work, surface wave SI is not further considered as a method for the following research.

The different SI methods utilising body waves will be considered one by one, starting with global-phase SI. The long ray paths of the earthquakes mean that the signal is significantly attenuated when it arrives. High frequencies are attenuated more, so the incoming signal has a low frequency content. This makes it a better fit for imaging of deeper, more pronounced discontinuities, like the Moho, but gives problems for smaller scale features. This can also be seen from the scale of previous research from table 1.
A second problem for the application of this method, is that it requires enough earthquakes of significant magnitude in the right region to occur during the recording time. For the Hellisheidi site, the range with epicentral distance larger than 120° is located roughly around the triple junction of the Antarctic, Australian and Pacific plates. This range includes part of the volcanic arc off New Zealand, a seismically active area. The survey took place over a week, which means that the likelihood of one earthquake of large enough magnitude happening is not high, let alone the minimum of 34 mentioned in table 1 to get a good azimuthal coverage.

The considerations for SI with teleseismic waves are very similar. The range for earthquakes is larger, containing epicentral distances between around 30 and 120°. In fact, one earthquake in this range (of M_W 8.2 in Alaska) happened during the recording time. It is still unlikely that there are earthquakes of significant magnitude from a good azimuthal coverage for proper imaging.

Ambient noise SI would be better suited for CO_2 monitoring. It requires less recording time and can image on the right scale. The main limitation is having to find body wave events to improve resolution. From the literature, beamforming analysis seems a good way to detect them. The different machine learning methods mentioned are interesting out of personal interest.
The noise should still come from sources spread around a larger area, for good coverage. The Hellisheidi site, and Iceland in general contain a lot of seismicity, providing ample sources from different directions. This also leads directly to the last method discussed.

Local earthquake SI finds a way between global earthquake and ambient noise SI. It can provide stronger local events that are distinct, but still provide a good resolution on reservoir scale. It requires a seismically active area, but the location of Iceland on the Atlantic rift and the associated volcanism provide enough activity. This makes the method especially well suited for the site. There are local sources providing body waves from different directions.
Microseismicity still has the problem that it can be obscured by other (surface wave) noise. Similar methods to those for ambient noise SI can be used to improve image quality.

6 Conclusion

Both ambient noise SI using body waves and SI using local seismicity are identified as useful methods to monitor subsurface CO_2 after reinjection at the Hellisheidi site in Iceland. They provide better image quality on reservoir scale and do not require long survey durations. Local seismic activity in Iceland allows for the use of the latter method and makes it the preferable one to use.

References

Abe, S., Kurashimo, E., Sato, H., Hirata, N., Iwasaki, T., & Kawanaka, T. (2007). Interferometric seismic imaging using scattered teleseismic waves. *Geophysical Research Letters*, *34*(L19305), 1–6. https://doi.org/10.1029/2007GL030633

Andrés, J., Draganov, D., Schimmel, M., Ayarza, P., Palomeras, I., Ruiz, M., & Carbonell, R. (2019). Lithospheric image of the Central Iberian Zone (Iberian Massif) using global-phase seismic interferometry. *Solid Earth*, *10*, 1937–1950. https://doi.org/10.5194/se-10-1937-2019

Bensen, G., Ritzwoller, M., Barmin, M., Levshin, A., Lin, F., Moschetti, M., Shapiro, N., & Yang, Y. (2007). Processing seismic ambient nosie data to obtain reliable borad-band surface wave dispersion measurements. *Geopysical Journal International*, *169*, 1239–1260. https://doi.org/10.1111/j.1365-246X.2007.03374.x

Benson, S. M., & Cole, D. R. (2008). CO_2 sequestration in deep sedimentary formations. *Elements*, *4*, 325–331. https://doi.org/10.2113/gselements.4.5.325

Bianchi, I., Ruigrok, E., Obermann, A., & Kissling, E. (2021). Moho topography beneath the European Eastern Alps by global-phase seismic interferometry. *Solid Earth*, *12*, 1185–1196. https://doi.org/10.5194/se-12-1185-2021

Boullenger, B., Verdel, A., Paap, B., Thorbecke, J., & Draganov, D. (2015). Studying CO_2 storage with ambient-noise seismic interferometry: A combined numerical feasibility study and field-data example for Ketzin, Germany. *Geophysics*, *80*(1), Q1–Q13. https://doi.org/10.1190/GEO2014-0181.1

Casas, J., Draganov, D., Badi, G., Manassero, M., Olivera Craig, V., Franco Marín, L., Gómez, M., & Ruigrok, E. (2019). Seismic interferometry applied to local fracture seismicity recorded at Planchón-Peteroa Volcanic Complex, Argentina-Chile. *Journal of South American Earth Sciences*, *92*, 134–144. https://doi.org/10.1016/j.jsames.2019.03.012

Casas, J. A., Badi, G. A., Franco, L., & Draganov, D. (2020). Seismic interferometry applied to regional and teleseismic events recorded at Planchón-Peteroa Volcanic Complex, Argentina-Chile. *Journal of Volcanology and Geothermal Research*, *393*(10685), 1–10. https://doi.org/10.1016/j.jvolgeores.2020.106805

Chamarczuk, M., Maliniowski, M., Nishitsuji, Y., Thorbecke, J., Koivisto, E., Heinonen, S., Juurela, S., Mężyk, M., & Draganov, D. (2019). Automatic 3D illumination-diagnosis method for large-N arrays: robust data scanner and machine-learning feature provider. *Geophysics*, *84*(3), Q13–Q25. https://doi.org/10.1190/GEO2018-0504.1

Chamarczuk, M., Nishitsuji, Y., Maliniowski, M., & Draganov, D. (2020). Unsupervised learning used in automatic detection and classification of ambient-noise recordings from a large-N array. *Seismological Research Letters*, *91*(1), 370–389. https://doi.org/10.1785/0220190063

Cheraghi, S., Craven, J. A., & Bellefleur, G. (2015). Feasibility of virtual source reflection seismology using interferometry for mineral exploration: A test study in the Lalor Lake volcanogenic massive sulphide mining area, Manitoba, Canada. *Geophysical Prospecting*, *63*, 833–848. https://doi.org/10.1111/1365-2478.12244

Claerbout, J. F. (1968). Synthesis of a layered medium from its acoustic transmission response. *Geophysics*, *33*(2), 264–269. https://doi.org/10.1190/1.1439927

Corciuolo, M., Roux, P., Campillo, M., Dubucq, D., & Kuperman, W. (2012). Multiscale matched-field processing for oise-source localization in exploration geophysics. *Geophysics*, *77*(5), KS33–KS41. https://doi.org/10.1190/GEO2011-0438.1

Daneshvar, M., Clay, C. S., & Savage, M. K. (1995). Passive seismic imaging using microearthquakes. *Geophysics*, *60*(4), 1178–1186. https://doi.org/10.1190/1.1443846

Draganov, D., Campman, X., Thorbecke, J., Verdel, A., & Wapenaar, K. (2009). Reflection images from ambient seismic noise. *Geophysics*, *74*, A63–A67. https://doi.org/10.1190/1.3193529

Draganov, D., Campman, X., Thorbecke, J., Verdel, A., & Wapenaar, K. (2013). Seismic exploration-scale velocities and structure from ambient seismic noise (>1 Hz. *Journal of Geophysical Research: Solid Earth*, *118*, 4345–4360. https://doi.org/10.1002/jgrb.50339

Draganov, D., & Ruigrok, E. (2014). Passive seismic interferometry for subsurface imaging. In M. Beer, I. A. Kougioumtzoglou, E. Patelli, & I. S.-K. Au (Eds.), *Encyclopedia of earthquake engineering* (pp. 1–13). Springer Berlin Heidelberg. https://doi.org/10.1007/978-3-642-36197-5_378-1

Durucan, S., Korre, A., Parlaktuna, M., Senturk, E., Wolf, K.-H., Chalari, A., Stork, A., Nikolov, S., de Kunder, R., Sigfusson, B., Hjörleifsdóttir, V., Andersen, N., & Poletto, F. (2021). SUCCEED: A CO_2 storage and utilisation project aimed at mitigating against greenhouse gas emissions from geothermal power production. https://doi.org/10.2139/ssrn.3819789

Eiken, O., Brevik, I., Arts, R., Lindeberg, E., & Fagervik, K. (2000). Seismic monitoring of CO_2 injected into a marine aquifer. *SEG Technical Program Expanded Abstracts 2000*, 1623–1626. https://doi.org/10.1190/1.1815725

Furre, A.-K., Eiken, O., Alnes, H., Vevatne, J. N., & Kiær, A. F. (2017). 20 years of monitoring CO_2-injection at Sleipner. *Energy Procedia*, *114*, 3916–3926. https://doi.org/10.1016/j.egypro.2017.03.1523

Haklidir, F., Baytar, K., & Kekevi, M. (2019). In H. Qudrat-Ullah & A. A. Kayal (Eds.), *Climate Change and Energy Dynamics in the Middle East. Understanding Complex Systems* (pp. 323–357). Springer International Publishing. https://doi.org/10.1007/978-3-030-11202-8_12

Ikeda, T., Tsuji, T., Nakatsukasa, M., Ban, H., Kato, A., Worth, K., White, D., & Roberts, B. (2018). Imaging and monitoring of the shallow subsurface using spatially windowed surface-wave analysis with a single permanent seismic source. *Geophysics*, *83*(6), EN23–EN38. https://doi.org/10.1190/GEO2018-0084.1

Ikeda, T., Tsuji, T., Watanabe, T., & Yamaoka, K. (2016). Development of surface-wave monitoring system for leaked CO_2 using a continuous and controlled seismic source. *International Journal of Greenhouse Gas Control*, *45*, 94–105. https://doi.org/10.1016/j.ijggc.2015.11.030

Kim, D., Brown, L. D., Árnason, K., Águstsson, K., & Blanck, H. (2017). Magma reflection imaging in Krafla, Iceland, using microearthquake sources. *Journal of Geophysical Research: Solid Earth*, *122*, 5228–5242. https://doi.org/10.1002/2016JB013809

Matter, M., Snaebjörnsdottir, S. Ó., Mesfin, K. G., Alfredsson, H. A., Hall, J., Arnarsson, M. T., Dideriksen, K., Júliusson, B. M., Broecker, W. S., & Gunnlaugsson, E. (2015). Towards cleaner geothermal energy: Subsurface sequestration of sour gas emissions from geothermal power plants.

Metz, B., Davidson, O., De Coninck, H., Loos, M., & Meyer, L. (2005). *IPCC special report on carbon dioxide capture and storage*. Cambridge University Press.

Nakata, N., Boué, P., Brenguier, F., Roux, P., Ferrazzini, V., & Campillo, M. (2016). Body and surface wave reconstruction from seismic noise correlations between arrays at Piton de la Fournaise volcano. *Geophysical Research Letters*, *43*, 1047–1054. https://doi.org/10.1002/2015GL066997

Nakata, N., Chang, J. P., & Lawrence, J. F. (2015). Body-wave extraction and tomography at Long Beach, CA, with ambient-noise interferometry. *Journal of Geophysical Research: Solid Earth*, *120*(2), 1159–1173. https://doi.org/10.1002/2015JB011870

Nakata, N., Snieder, R., Tsuji, T., Larner, K., & Matsuoka, T. (2011). Shear wave imaging from traffic noise using seismic interferometry by cross-coherence. *Geophysics*, *76*(6), SA97–SA106. https://doi.org/10.1190/GEO2010-0188.1

Nishitsuji, Y., Minato, S., Boullenger, B., Gomez, M., Wapenaar, K., & Draganov, D. (2016). Crustal-scale reflection imaging and interpretation by passive seismic interferometry using local earthquakes. *Interpretation*, *4*(3), SJ29–SJ53. https://doi.org/10.1190/INT-2015-0226.1

Nishitsuji, Y., Rowe, C., Wapenaar, K., & Draganov, D. (2016). Reflection imaging of the Moon's interior using deep-moonquake seismic interferometry. *Journal of Geophysical Research: Planets*, *121*, 695–713. https://doi.org/10.1002/2015JE004975

Nishitsuji, Y., Ruigrok, E., Gomez, M., Wapenaar, K., & Draganov, D. (2016). Reflection imaging of aseismic zones of the Nazca slab by global-phase seismic interferometry. *Interpretation*, *4*(3), SJ1–SJ16. https://doi.org/10.1190/INT-2015-0225.1

Panea, I., Draganov, D., Almagro Vidal, C., & Mocanu, V. (2014). Retrieval of reflections from ambient noise recorded in the Mizil area, Romania. *Geophysics*, *79*(3), Q31–Q42. https://doi.org/10.1190/GEO2013-0292.1

Polychronopoulou, K., Lois, A., & Draganov, D. (2020). Body-wave passive seismic interferometry revisited: mining exploration using the body waves of local microearthquakes. *Geophysical prospecting*, *68*, 232–253. https://doi.org/10.1111/1365-2478.12884

Roots, E., Calvert, A. J., & Craven, J. (2017). Interferometric seismic imaging around the active Lalor mine in the Flin Flon greenstone belt, Canada. *Tectonophysics*, *718*, 92–104. https://doi.org/10.1016/j.tecto.2017.04.024

Ruigrok, E., Campman, X., & Wapenaar, K. (2011). Extraction of P-wave reflections from microseisms. *Comptes Rendus Geoscience*, *343*, 512–525. https://doi.org/10.1016/j.crte.2011.02.006

Ruigrok, E., & Wapenaar, K. (2012). Global-phase seismic interferometry unveils P-wave reflectivity below the Himalayas and Tibet. *Geophysical Research Letters*, *39*(L11303), 1–6. https://doi.org/10.1029/2012GL051672

Sabra, K. G., Gerstoft, P., Roux, P., Kuperman, W., & Fehler, M. C. (2005). Surface wave tomography from microseisms in Southern California. *Geophysical Research Letters*, *32*(L14311), 1–4. https://doi.org/10.1029/2005GL023155

Sass, J., & Duffield, W. (2003). *Geothermal energy: Clean power from the earth's heat*. DIANE Publishing.

Scherbaum, F. (1987). Seismic imaging of the site response using microearthquake recordings. Part I Method. *Bulletin of the Seismological Society of America*, *77*(6), 1905–1923. https://doi.org/10.1785/BSSA0770061905

Schuster, G. (2009). *Seismic interferometry*. Cambridge University Press. https://doi.org/10.1017/CBO9780511581557

Shapiro, N. M., & Campillo, M. (2004). Emergence of broadband Rayleigh waves form correlations of the ambient seismic noise. *Geophysical Research Letters*, *31*(L07614), 1–1. https://doi.org/10.1029/2004GL019491

Shapiro, N. M., Campillo, M., Stehly, L., & Ritzwoller, M. H. (2005). High-resolution surface-wave tomography from ambient seismic noise. *Science*, *307*, 1615–1618. https://doi.org/10.1126/science.1108339

Sigfusson, B., Gislason, S. R., Matter, J. M., Stute, M., Gunnlaugsson, E., Gunnarsson, I., Aradottir, E. S., Sigurdardottir, H., Mesfin, K., Alfredsson, H. A., Wolff-Boensich, D., Arnarsson, M. T., & Oelkers, E. H. (2015). Solving the carbon-dioxide buoyancy challenge: The design and field testing of a dissolved CO_2 injection system. *International Journal of Greenhouse Gas Control*, *37*, 213–219. https://doi.org/10.1016/j.ijggc.2015.02.022

Snieder, R. (2004). Extracting the Green's function from the correlation of coda waves: A derivation based on stationary phase. *Physical Review*, *69*(046610), 1–8. https://doi.org/10.1103/PhysRevE.69.046610

Stein, S., & Wysession, M. (2003). *An introduction to seismology, earthquakes and earth structure*. Blackwell Publishing.

Stork, A. L., Chalari, A., Durucan, S., Korre, A., & Nikolov, S. (2020). Fibre-optic monitoring for high-temperature Carbon Capture, Utilization and Storage (CCUS) projects at geothermal energy sites. *First Break*, *38*, 61–67. https://doi.org/10.3997/1365-2397.fb2020075

Tonegawa, T., Nishida, K., Watanabe, T., & Shiomi, K. (2009). Seismic interferometry of teleseismic S-wave coda for retrieval of body waves: an application to the Philippine Sea slab underneath the Japanese Islands. *Geophysical Journal International*, *178*, 1574–1586. https://doi.org/10.1111/j.1365-246X.2009.04249.x

Wapenaar, K., Draganov, D., Snieder, R., Campman, X., & Verdel, A. (2010). Tutorial on seismic interferometry: Part 1 - basic principles and applications. *Geophysics*, *75*(5), 195–209. https://doi.org/10.1190/1.3457445

Wapenaar, K., & Fokkema, J. (2006). Green's functions representations for seismic interferometry. *Geophysics*, *71*(4), 33–46. https://doi.org/10.1190/1.2213955

Wapenaar, K., Thorbecke, J., & Draganov, D. (2004). Relations between reflection and transmission responses of three-dimensional inhomogeneous media. *Geophysical Journal International*, *156*, 179–194. https://doi.org/10.1111/j.1365-246X.2003.02152.x

Whittaker, S., Rostron, B., Hawkes, C., Gardner, C., White, D., Johnson, J., Chalaturnyk, R., & Seeburger, D. (2011). A decade of CO_2 injection into depleting oil fields: monitoring and research activities of the IEA GHG Weyburn-Midale CO_2 monitoring and storage project. *Energy Procedia*, *4*, 6069–6076. https://doi.org/10.1016/j.egypro.2011.02.612

Yang, Y., Ritzwoller, H., Michael, Levshin, A. L., & Shapiro, N. M. (2007). Ambient noise Rayleigh wave tomography across Europe. *Geophysical Journal International*, *168*, 259–274. https://doi.org/10.1111/j.1365-246X.2006.03203.x